Agricultural Water Management 325 (2026) 110153

Contents lists available at ScienceDirect

Agricultural Water Management

journal homepage: www.elsevier.com/locate/agwat

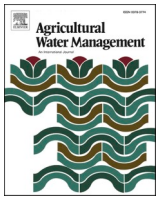

Stomatal conductance modeling for drip-irrigated kiwifruit in seasonal drought regions of South China: Evaluation of improved empirical models and interpretable machine learning approaches

Shunsheng Zheng [a], Ningbo Cui [a,*], Quanshan Liu [a], Shouzheng Jiang [a], Daozhi Gong [b], Xiaoxian Zhang [c]

[a] State Key Laboratory of Hydraulics and Mountain River Engineering & College of Water Resource and Hydropower, Sichuan University, Chengdu 610065, China
[b] Institute of Environment and Sustainable Development in Agriculture, Chinese Academy of Agricultural Sciences, Beijing 100081, China
[c] Sustainable Soils and Crops, Rothamsted Research, Harpenden, England AL5 2JQ, UK

ARTICLE INFO

Keywords:
Soil water deficit
Kiwifruit vine
Stomatal conductance model
Growth stage
CatBoost

ABSTRACT

Accurate modeling of stomatal conductance (g_s) enhances understanding of plant water relations and supports advancements in eco-physiological modeling and adaptive irrigation practices. This study provides a comprehensive evaluation of g_s modeling for drip-irrigated kiwifruit through parallel development of three Jarvis-type empirical models (JV, JV1, JV2) and five machine learning algorithms (XGBoost, LightGBM, CatBoost, SVR, LR) based on three years of field measurements comprising synchronized records of g_s and key environmental drivers. Models were assessed via year-wise grouped cross-validation, with performance measured by R^2, RMSE, and MAE, and interpretability analyzed using SHapley Additive exPlanations (SHAP) and Partial Dependence Plots (PDPs). Results showed that deficit irrigation significantly reduced g_s, with sensitivity being most pronounced during stage II. The incorporation of soil water content (SWC) substantially improved the accuracy of both empirical and machine learning models. Among empirical models, JV2, featuring a stage-specific nonlinear SWC response function, demonstrated the highest accuracy (R^2 ranging from 0.736 to 0.814) and minimized bias under extreme SWC conditions. Using vapor pressure deficit (VPD), air temperature (Ta), photosynthetically active radiation (PAR), and SWC as input variables, CatBoost outperformed both empirical models and other machine learning algorithms across all growth stages (R^2 = 0.815–0.839; RMSE = 0.065–0.076 mol m^{-2} s^{-1}; MAE = 0.054–0.064 mol m^{-2} s^{-1}). SHAP analysis and PDPs identified VPD as the dominant driver of g_s variation, followed by SWC. Overall, the improved JV2 model offers a structurally transparent framework for g_s estimation with acceptable accuracy, while CatBoost combined with SHAP analysis and PDPs provides superior predictive performance and robust interpretability under complex environmental conditions. These findings support the reliable modeling and regulation of kiwifruit g_s under varying SWC scenarios in drip-irrigated orchards.

1. Introduction

With rising global temperatures and increasingly frequent drought events, agricultural systems face unprecedented challenges in sustaining crop productivity and water use efficiency (Houshmandfar et al., 2021). Stomata are microscopic pores on the leaf surface that regulate transpiration. They also facilitate CO_2 uptake for photosynthesis, serving as a key physiological interface between plants and the atmosphere (Buckley, 2019; Gaur and Drewry, 2024). Stomatal conductance (g_s), a measure of the degree of stomatal opening, is widely recognized as an essential indicator of plant water status and response to drought stress (Martin-Stpaul, 2017). Accurate modeling of g_s is crucial for simulating plant-atmosphere interactions within land surface and crop growth models. Stomata directly control transpiration rates, which constitute a major component of evapotranspiration. Consequently, reliable g_s estimation significantly enhances the accuracy of ET modeling and water flux quantification (Franks et al., 2018; Wang et al., 2018). In agro-ecosystems, especially under water-limited conditions, reliable g_s modeling enhances the estimation of evapotranspiration and supports the development of precise irrigation strategies (Houshmandfar et al.,

* Corresponding author.
E-mail address: cuiningbo@126.com (N. Cui).

https://doi.org/10.1016/j.agwat.2026.110153
Received 7 August 2025; Received in revised form 24 November 2025; Accepted 10 January 2026
Available online 16 January 2026

2021; Wu et al., 2021).

Stomatal conductance models are typically classified into empirical, semi-empirical, and mechanistic types (Li et al., 2023). Among these, the Jarvis model is one of the most widely used empirical models, due to its simplicity, ease of parameterization, and robust performance across various plant types, such as crops, fruit trees, and forests (Houshmandfar et al., 2021; Wu et al., 2021; Wang et al., 2018). It expresses g_s as the product of normalized response functions that represent the effects of individual environmental variables, including photosynthetically active radiation (PAR), vapor pressure deficit (VPD), air temperature (Ta), and atmospheric CO_2 concentration (C_a) (Jarvis, 1976). However, the original formulation did not explicitly consider water stress or relied on leaf water potential, which is difficult to measure under field conditions. To address this, subsequent studies introduced soil water content (SWC) as an indicator of plant water status and incorporated SWC response functions (Houshmandfar et al., 2021). Nevertheless, the commonly used three-stage linear approach fails to adequately capture the nonlinear and saturating nature of the g_s–SWC relationship, especially under extreme SWC conditions, reducing model accuracy under dynamic SWC conditions (Qi et al., 2023; Wu et al., 2021). To address this gap, the present work develops and tests a novel, stage-specific nonlinear SWC response function derived from boundary line analysis. This approach is designed to better represent the physiological thresholds of kiwifruit vines and to improve model performance across a wider range of SWC conditions compared to traditional linear formulations.

Machine learning models have shown notable advantages in modeling crop responses to environmental factors, particularly in scenarios involving nonlinear relationships and complex interactions among multiple variables. For instance, random forest models have demonstrated excellent performance in predicting evaporation rates in complex environmental systems (Al-Mahdawi et al., 2023). Ensemble algorithms such as XGBoost, LightGBM, and CatBoost have been widely applied in agricultural and ecological studies, demonstrating high prediction accuracy (Ellsäßer et al., 2020; Gaur and Drewry, 2024; Saunders et al., 2021). However, their application in modeling g_s remains limited. Moreover, conventional machine learning models are often regarded as "black-box" systems due to their lack of physiological interpretability (Lundberg and Lee, 2017; Hussein and Abouessaouab, 2023). To address this limitation, model interpretation methods such as SHapley Additive exPlanations (SHAP) have been introduced to quantify the influence of each input variable on model predictions (Yu et al., 2025). In recent years, SHAP has been effectively utilized in agricultural and environmental sciences to identify key drivers of crop yield, evapotranspiration patterns, and soil quality indicators (Dhawi et al., 2025; Mohammed et al., 2024; Rahimi et al., 2025). Integrating machine learning models with SHAP analysis presents promising opportunities for enhancing g_s simulation accuracy while uncovering underlying environmental response mechanisms.

Kiwifruit is an important economic fruit crop known for its high nutritional value and unique flavor (Wang et al., 2021). China contributes to over 40 % of the global kiwifruit cultivation area, with more than half located in southern China where seasonal drought and fluctuating irrigation water availability are common (Zheng et al., 2025). While stomatal conductance modeling has been advanced for other fruit crops such as grapes (Sun et al., 2023) and apple (Miao et al., 2021), the mechanisms by which g_s responds to environmental factors and SWC in kiwifruit remain insufficiently understood. Previous studies on kiwifruit have primarily focused on yield and quality responses to water deficit (Calderón-Orellana et al., 2025; Zheng et al., 2023), with limited attention to mechanistic modeling of stomatal behavior. This gap constrains the optimization of water management strategies and undermines the accuracy of evapotranspiration estimation, carbon assimilation simulation, and eco-physiological modeling. Therefore, this study aimed to investigate the response of kiwifruit g_s to varying SWC under drip irrigation and develop accurate modeling approaches. The specific objectives were to: 1) quantify the stage-specific response patterns of kiwifruit g_s to varying SWC; 2) develop an improved Jarvis-type empirical model by incorporating a novel, stage-specific nonlinear soil water response function; 3) evaluate the performance of multiple machine learning algorithms in predicting kiwifruit g_s; 4) identify the key environmental drivers of g_s variation and interpret their effects. The findings are expected to improve the accuracy and interpretability of g_s simulation, contributing to a physiologically informed modeling framework for precision irrigation in drip-irrigated kiwifruit orchards.

2. Materials and methods

2.1. Experimental site and design

Field experiments were carried out at the kiwifruit experimental station from 2017 to 2019. The experimental site was located in Chengdu City, Sichuan Province, China (30°19'20"N, 103°25'57"E), within a subtropical monsoon climate zone. The terrain of the area is characterized by shallow hills, and the dominant soil type is yellow earth, consisting of 10.9 % sand, 76.8 % silt, and 12.3 % clay. The average soil bulk density was 1.27 g cm^{-3}, with a field capacity (FC) of 0.383 m^3 m^{-3} and a permanent wilting point (PWP) of 0.145 m^3 m^{-3}.

Eight-year-old kiwifruit vines (*Actinidia chinensis* 'Jinyan'), a yellow-fleshed cultivar, were selected for this study. The vines were planted with a row spacing of 5.0 m and a plant spacing of 4.5 m. The growth period was divided into four distinct developmental stages: bud burst to leafing stage (I, mid-March to mid-April), flowering to fruit set stage (II, mid-April to early May), fruit expansion stage (III, early May to late June), and fruit maturation stage (IV, late June to late October). Five irrigation levels were implemented, including one full irrigation control (CTL) and four levels of deficit irrigation: low (D15 %), mild (D25 %), moderate (D35 %), and severe (D45 %), corresponding to 85 %, 75 %, 65 %, and 55 % of full irrigation amount, respectively. Irrigation scheduling was based on crop water requirements (ET_c), which were estimated using the single crop coefficient method. Reference evapotranspiration (ET_0) was calculated using the Penman-Monteith function (Allen et al., 1998). Kiwifruit crop coefficients (K_c) were calibrated by Jiang et al. (2022) and determined to be 0.98, 1.26, 1.36, and 1.21 for stages I to IV, respectively. A completely randomized design was adopted, with three independent replicates per treatment. Each experimental plot consisted of five vines, with the two edge vines serving as border plants and the three central vines as experimental plants. Drip irrigation was employed, with two lateral drip lines installed along each plant row. The drip lines were equipped with pressure-compensating emitters with a flow rate of 1.6 L h^{-1}, spaced at 0.4 m intervals.

2.2. Measurement

Stomatal conductance (g_s) and environmental parameters were measured using a portable photosynthesis system (LCPro-SD, ADC BioScientific, UK). For each treatment, one representative vine was selected. On each selected vine, six fully expanded and healthy leaves were randomly chosen from the upper-middle canopy for measurement. To capture g_s responses under conditions of significant variation in soil moisture and environmental factors, measurements were conducted on two separate days during each growth stage—one day prior to irrigation and one day following irrigation. On each measurement day, g_s and environmental parameters, including photosynthetically active radiation (PAR, μmol m^{-2} s^{-1}), air temperature (Ta, ℃), relative humidity (RH, %), and vapor pressure deficit (VPD, kPa), were recorded at 2-hour intervals from 9:00–17:00 under clear sky conditions.

Volumetric soil water content (SWC) was monitored using PR2 profile probes (PR2/6, Delta-T Devices Ltd., UK), which were installed at a distance of 10 cm from the emitters in each plot. The probes collected SWC data at five depths: 10, 20, 30, 40, and 60 cm, covering the effective rooting zone of kiwifruit. The average SWC across all five depths was

used to represent the overall soil moisture status. The sensors were factory-calibrated and further validated against gravimetric SWC measurements to ensure measurement accuracy.

2.3. Boundary line approach

The boundary line approach analyzes the relationship between a single dependent variable and an independent variable under complex conditions (Alonso et al., 2008). It assumes that the outer margin data points represent the functional relationship between the two factors, specifically SWC and g_s in this study. At this margin, SWC is considered the sole limiting factor for g_s; data below it suggests additional influencing factors. To define the boundary, g_s data were grouped into SWC classes with 0.005 cm^3 cm^{-3} increments. The maximum g_s value was calculated as the average of values above the 95th percentile (Alonso et al., 2008), while the average SWC per class was derived from all data in that class. A function was then fitted to relate maximum g_s and average SWC.

2.4. Empirical stomatal conductance model

The Jarvis model assumes that the effects of PAR, VPD, Ta, and atmospheric CO_2 concentration (Ca) on g_s are independent, and it represents g_s as the product of these environmental factors (Jarvis, 1976):

$$g_s = g_{s\,max} \cdot f(PAR) \cdot f(VPD) \cdot f(T_a) \cdot f(Ca) \tag{1}$$

where g_{smax} denotes the maximum stomatal conductance under non-limiting conditions (mol m^{-2} s^{-1}), and f(PAR), f(VPD), f(Ta), and f(Ca) are dimensionless reduction functions (0–1) describing the responses of g_s to PAR, VPD, Ta, and Ca, respectively. In this study, Ca showed minimal variation across seasons and within days and was therefore omitted. The formulations for f(PAR), f(VPD), and f(Ta) were adopted from Samanta et al. (2008) and Matsumoto et al. (2005), and Ortega-Farias et al. (2010), respectively, and are expressed as follows:

$$f(PAR) = \frac{PAR}{PAR + k_1} \tag{2}$$

$$f\left(VPD\right) = \frac{1}{1 + \left(\frac{VPD}{VPD_{0.5}}\right)^{k_2}} \tag{3}$$

$$f(T_a) = 1 - k_3\left(T_a - T_{opt}\right)^2 \tag{4}$$

where $VPD_{0.5}$ is the VPD value when f(VPD) is equal to 0.5; T_{opt} is the fitted optimum temperature; k_1, k_2, and k_3 are empirical parameters.

2.4.1. Traditional soil water response function

Stomata opening is notably influenced by SWC variations. A commonly used soil water response function is a three-stage linear formulation based on PWP and FC, referred to as f_1(SWC) (Eq. 5) (Qi et al., 2023):

$$f_1(SWC) = \begin{cases} 0 & \text{SWC} < \text{PWP} \\ \dfrac{SWC - PWP}{FC - PWP} & \text{PWP} < \text{SWC} < \text{FC} \\ 1 & \text{FC} < \text{SWC} \end{cases} \tag{5}$$

where PWP and FC are SWC at permanent wilting point and field capacity, respectively. This function assumes that g_s increases linearly with SWC between PWP and FC and reaches its maximum value when SWC exceeds FC. Although simple and widely used, this linear assumption does not fully reflect the nonlinear and saturating behavior observed in g_s–SWC relationship between PWP and FC (Qi et al., 2023; Wang et al., 2018).

2.4.2. Improved soil water response function

Field observations in this study indicated that the relationship between g_{smax} and SWC is better characterized by a nonlinear pattern with a decline at low SWC and a saturation plateau at high SWC. To capture this behavior, an improved soil water response function f_2(SWC) was developed based on the boundary line approach described in Section 2.3. For each growth stage, the upper envelope of the measured g_s–SWC scatter distribution was extracted, and two physiologically meaningful thresholds were identified: 1) the lower SWC threshold (SWC_{sc}) at which stomata closure occurs and g_s approaches zero; and 2) the upper SWC threshold (SWC_t) at which g_s reaches its maximum and becomes insensitive to further increases in SWC. Based on these thresholds, f_2(SWC) was defined as a piecewise linear function:

$$f_2(SWC) = \begin{cases} 0 & \text{SWC} < \text{SWC}_{sc} \\ \dfrac{SWC - SWC_{sc}}{SWC_t - SWC_{sc}} & \text{SWC}_{sc} < \text{SWC} < SWC_t \\ 1 & SWC_t < \text{SWC} \end{cases} \tag{6}$$

Below SWC_{sc}, stomata are considered effectively closed and g_s is zero. Between SWC_{sc} and SWC_t, g_s increases approximately linearly with SWC, representing the transition from water-stressed to adequately watered conditions. When SWC exceeds SWC_t, f_2(SWC) remains equal to 1, indicating a saturation region where soil water is no longer limiting to g_s. In contrast to f_1(SWC), which relies solely on static soil hydraulic limits (PWP and FC), the thresholds SWC_{sc} and SWC_t in f_2(SWC) are derived from data-driven boundary line analysis. This approach represents a fundamental shift from a soil-centric to a plant-physiology-centric framework, as it incorporates stage-specific physiological responses and directly captures the observed nonlinear saturation behavior of stomata. The estimated threshold values for each growth stage are presented in the Results section.

2.4.3. Jarvis-type model configurations

Based on the above response functions, three Jarvis-type empirical stomatal conductance models were constructed:

$$JV = g_{s\,max} \cdot f(PAR) \cdot f(VPD) \cdot f(T_a) \tag{7}$$

$$JV1 = g_{s\,max} \cdot f(PAR) \cdot f(VPD) \cdot f(T_a) \cdot f_1(SWC) \tag{8}$$

$$JV2 = g_{s\,max} \cdot f(PAR) \cdot f(VPD) \cdot f(T_a) \cdot f_2(SWC) \tag{9}$$

The JV model represents the original Jarvis formulation without a soil water term. JV1 incorporates the traditional soil water response function f_1(SWC), whereas JV2 employs the improved stage-specific function f_2(SWC).

2.5. Machine learning algorithm and SHAP and partial dependence analysis

Five machine learning algorithms were used to estimate g_s, including eXtreme Gradient Boosting (XGBoost), Light Gradient Boosting Machine (LightGBM), Categorical Boosting (CatBoost), Support Vector Regression (SVR), and Linear Regression (LR). These algorithms were chosen to represent a spectrum of ensemble-based, kernel-based, and parametric learning strategies, each exhibiting distinct advantages in addressing nonlinearity, feature interactions, and interpretability.

XGBoost is an efficient implementation of gradient-boosted decision trees. It constructs an ensemble of weak learners in a sequential manner, aiming to minimize a regularized loss function in order to prevent overfitting and enhance generalization performance. XGBoost employs second-order derivatives for optimization and provides built-in support for handling missing values and parallel computation, making it particularly suitable for high-dimensional and nonlinear problems (Sheridan et al., 2016).

LightGBM, another gradient boosting framework, introduces

histogram-based feature binning and leaf-wise tree growth strategies, which significantly accelerate training speed while reducing memory consumption. This makes LightGBM highly effective for processing large-scale datasets and imbalanced data distributions (Pan et al., 2021).

CatBoost is a gradient boosting framework specifically designed for handling categorical data and performing well on small-to-medium-sized datasets. It integrates ordered boosting and permutation-driven techniques to reduce prediction shift and mitigate overfitting (Dorogush et al., 2018). Additionally, CatBoost offers native support for missing value imputation and categorical feature encoding, thereby simplifying the preprocessing pipeline.

SVR is based on the theoretical foundation of support vector machines. It transforms input features into a high-dimensional feature space using kernel functions and seeks to find a flat regression function within a predefined tolerance margin (Ge et al., 2013). SVR is widely recognized for its robustness in modeling nonlinear relationships with limited sample sizes.

LR, as a baseline parametric model, assumes a linear relationship between the input predictor variables and the target variable (Fernandes and Leblanc, 2005). Despite its simplicity, LR remains valuable for interpretability and serves as a benchmark for evaluating more sophisticated models.

SHapley Additive exPlanations (SHAP) is a unified approach for explaining model outputs, which computes the marginal contribution of each feature using principles from cooperative game theory (Enouen and Liu, 2025). SHAP values provide both global and local interpretability, enabling the quantification of feature importance.

In addition to SHAP, partial dependence plots (PDPs) were used to characterize the marginal effects of individual environmental variables on g_s. Following Elshaarawy (2025), PDPs quantify the expected change in model predictions when a target variable varies across its observed range while all other variables are held at their empirical distributions. This method provides graphical representations that visualize the relationship between input features and the predicted outcome, averaging out the effects of other features to reveal how changes in a specific feature influence the model's predictions. PDPs are particularly useful for understanding the direction and magnitude of feature influence, enabling interpretation of whether the relationship is linear, monotonic, or more complex.

2.6. Model implementation and evaluation

2.6.1. Year-wise grouped three-fold cross-validation

To avoid temporal autocorrelation and information leakage, the dataset was not randomly shuffled. Instead, a year-wise blocked strategy was applied in which all measurements collected within the same year were treated as an indivisible group. Based on this grouping structure, a three-fold cross-validation was conducted using the measurement years as independent folds. In each fold, one year was used exclusively as the testing set, while the remaining two years served as the training set: train on 2017 and 2018 and test on 2019 (Fold 1); train on 2017 and 2019 and test on 2018 (Fold 2); and train on 2018 and 2019 and test on 2017 (Fold 3). This grouped validation design preserves the temporal dependence inherent in field measurements, prevents information leakage between folds, and enables an unbiased assessment of model generalization under unseen environmental and physiological conditions.

2.6.2. Calibration of Jarvis-type models

For the empirical models (JV, JV1, and JV2), parameters were estimated using constrained nonlinear optimization. The sum of squared errors between measured and simulated g_s was used as the objective function, and the trust-region-reflective algorithm implemented in MATLAB (lsqcurvefit) was used to obtain parameter solutions. For JV2, the two SWC thresholds (SWC_{sc} and SWC_t) were fixed based on the boundary-line analysis described in Section 2.3, while all remaining parameters (g_{smax}, $VPD_{0.5}$, T_{opt}, k_1, k_2, and k_3) were optimized jointly. To ensure that simulations remained physiologically meaningful, specific constraints were applied: g_{smax} was constrained to be no lower than the maximum observed g_s within each growth stage, and T_{opt} was restricted to fall within the range of 0–50 ℃.

2.6.3. Training of machine learning models

Prior to the training of machine learning models, all input variables (PAR, Ta, VPD, and SWC) were normalized to a common scale using min-max normalization. This preprocessing step is crucial for algorithms sensitive to feature scales, such as SVR and LR, and ensures a consistent basis for fair performance comparison across all evaluated machine learning models.

Hyperparameter tuning for the five machine learning models (XGBoost, LightGBM, CatBoost, SVR, and linear regression) was performed within the same year-wise three-fold grouped cross-validation framework to maintain consistency with the empirical model evaluation and to prevent overfitting by testing on temporally independent data. For the CatBoost model, hyperparameters were tuned using a manual, model-driven adjustment strategy. Based on preliminary experiments, the number of boosting iterations and learning rate were empirically adjusted to balance predictive accuracy and computational efficiency, while other hyperparameters including L2 regularization (l2_leaf_reg) were maintained at their default values due to CatBoost's built-in robustness against overfitting. The final configuration consisted of 200 iterations with a learning rate of 0.08. This approach aligns with established practices, as CatBoost's default settings often yield competitive performance without extensive hyperparameter searches, thereby enhancing reproducibility without compromising model effectiveness (Florek and Zagdański, 2023).

2.6.4. Performance metrics

Model performance was evaluated using the coefficient of determination (R^2), root mean square error (RMSE), mean absolute error (MAE), and relative residual:

$$R^2 = 1 - \frac{\sum_{i=1}^{n}(y_i - x_i)^2}{\sum_{i=1}^{n}(y_i - \bar{y})^2} \tag{10}$$

$$RMSE = \sqrt{\frac{1}{n}\sum_{i=1}^{n}(y_i - x_i)^2} \tag{11}$$

$$MAE = \frac{1}{n}\sum_{i=1}^{n}|y_i - x_i| \tag{12}$$

$$Relativeresidual = \frac{x_i - y_i}{y_i} \tag{13}$$

where y_i indicates the measured value, $\bar{y}$ indicates the mean measured value, x_i indicates the predicted value, and n is the sample size. Larger R^2 and smaller RMSE and MAE indicate better simulation performance of models, while relative residuals closer to zero indicate better local prediction accuracy across varying conditions. The methodological flowchart adopted in this study is presented in Fig. 1.

2.7. Statistical analysis

The significance of differences in g_s among irrigation treatments within each growth stage was determined using one-way analysis of variance (ANOVA). When the ANOVA indicated a significant effect ($p < 0.05$), post hoc comparisons were performed using Tukey's Honest Significant Difference (HSD) test to control the family-wise error rate.

To examine potential multicollinearity among environmental variables, the Variance Inflation Factor (VIF) was calculated for each growth

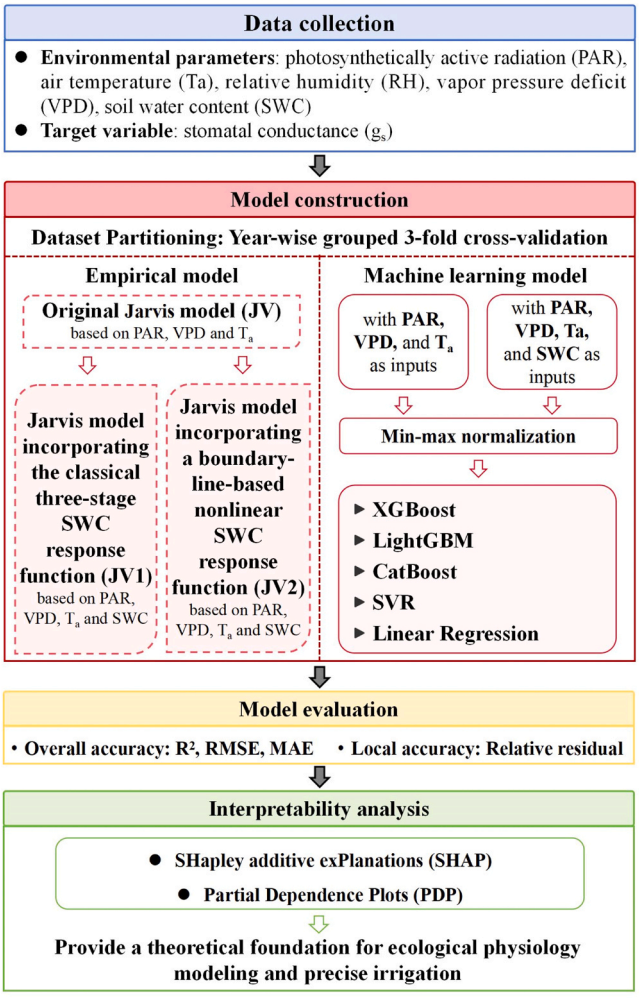

Fig. 1. Methodological flowchart adopted in this study.

stage. VIF values were computed using a linear regression framework, where a VIF greater than 10 was considered indicative of severe multicollinearity, and values between 5 and 10 suggested moderate multicollinearity. This analysis ensured that subsequent model interpretations and variable attribution results were not biased by redundant information among predictors.

To quantify the relative importance of environmental factors in regulating g_s, a one-way ANOVA was performed for each growth stage. Environmental variables were grouped using tertile-based thresholds (low, medium, and high) to ensure balanced sample sizes across categories. Prior to ANOVA, Levene's test was conducted to assess the homogeneity of variances. In addition to significance testing, the effect size (η^2) was calculated to quantify the magnitude of influence of each factor on g_s. These analyses provided a statistical basis for understanding the dominant drivers of g_s variations prior to predictive model development.

3. Results and analysis

3.1. Variations in soil water content and stomatal conductance of kiwifruit under deficit drip irrigation

The variations in SWC of kiwifruit under deficit drip irrigation are presented in Fig. 2. During stages I–IV, SWC under different irrigation levels ranged between 0.234–0.327, 0.243–0.345, 0.233–0.375, and 0.225–0.349 cm^3 cm^{-3}, respectively. It is evident that SWC increased with rising irrigation levels. Compared to CTL, deficit irrigation resulted in average reductions in SWC by 2.6–8.6 %, 3.9–10.8 %, 4.8–14.6 %, and 5.7–17.1 % during stages I–IV, respectively.

The variations and distribution of g_s in kiwifruit under deficit drip irrigation are illustrated in Fig. 3. As the growth period progressed, g_s exhibited a slightly increasing trend. During stages I–IV, g_s ranged between 0.04–0.79, 0.06–0.89, 0.08–0.97, and 0.08–0.90 mol m^{-2} s^{-1}, respectively. Although the overall ranges among treatments were similar, both the median and interquartile range (IQR) decreased with reduced irrigation levels at each stage. During stages I and II, g_s under CTL exhibited a bimodal distribution with relatively uniform density across low and high values, whereas deficit treatments showed a strong concentration of density toward the lower range. During stages III and IV, all treatments displayed unimodal distributions; however, the density peak shifted downward as deficit severity increased. Quantitatively, compared to CTL, the D45 % treatment significantly decreased average g_s by 20.5, 16.4, 20.1, and 25.4 % during stages I–IV ($p < 0.05$), respectively; the D35 % treatment showed significant reductions only in stages III and IV, decreasing average g_s by 15.3 % and 20.1 % ($p < 0.05$), respectively.

3.2. Multicollinearity and environmental controls on stomatal conductance

VIF analysis showed negligible collinearity for PAR and SWC across all growth stages, with VIF values consistently close to 1 (Table 1). In contrast, Ta and VPD exhibited elevated VIFs (6.14–9.14) during stages I–III, reflecting their inherent atmospheric coupling. Nevertheless, all VIF values were below the threshold of 10, indicating that collinearity among the environmental variables was not severe.

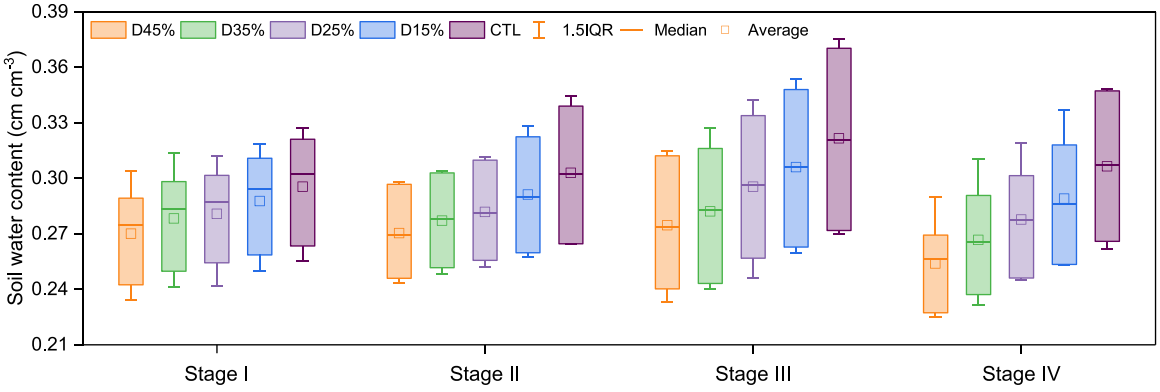

Fig. 2. Variations of soil water content of kiwifruit under deficit drip irrigation. I, II, III, and IV refer to bud burst to leafing stage, flowering to fruit set stage, fruit expansion stage, and fruit maturation stage, respectively. D45 %, D35 %, D25 %, and D15 % were water deficit levels where irrigated at 55 %, 65 %, 75 %, and 85 % of full irrigation (CTL), respectively.

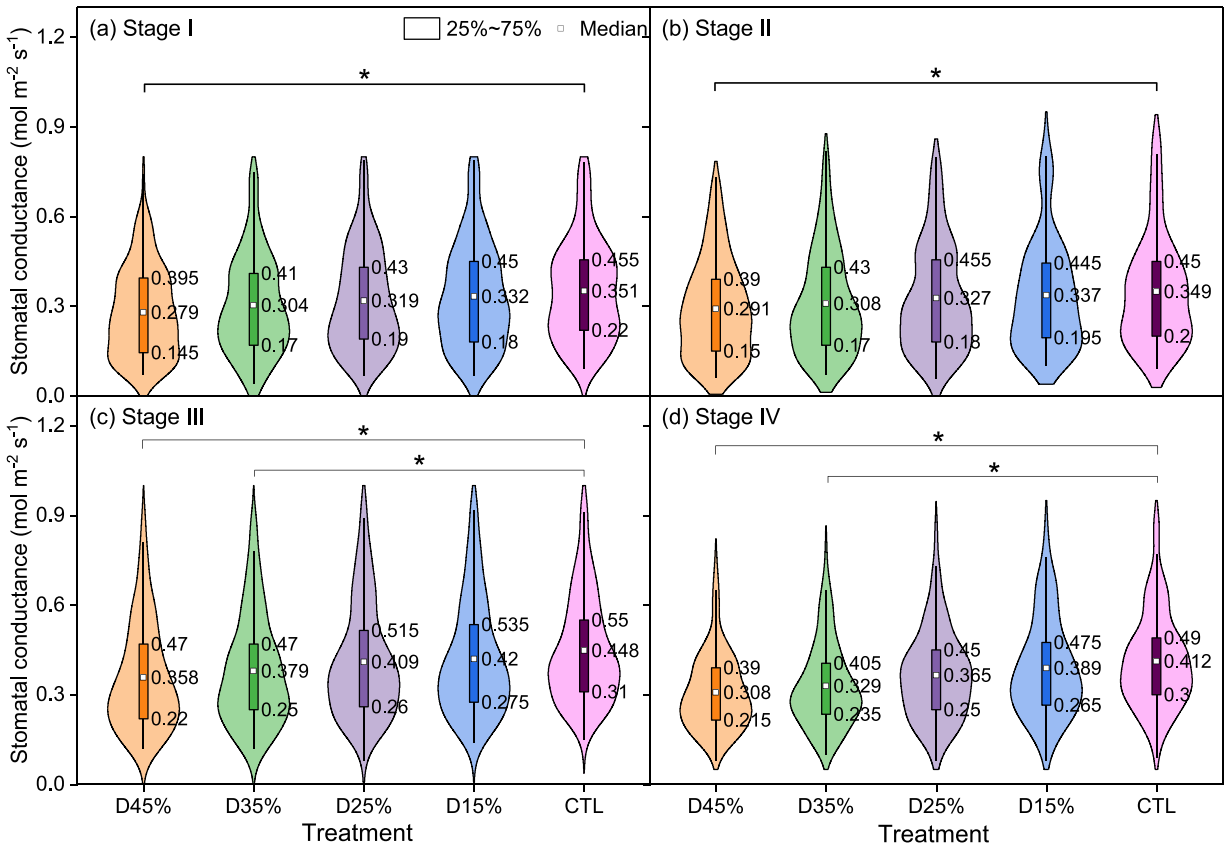

Fig. 3. Violin plots of stomatal conductance of kiwifruit under deficit drip irrigation across different growth stages. I, II, III, and IV refer to bud burst to leafing stage, flowering to fruit set stage, fruit expansion stage, and fruit maturation stage, respectively. D45 %, D35 %, D25 %, and D15 % were water deficit levels where irrigated at 55 %, 65 %, 75 %, and 85 % of full irrigation (CTL), respectively. * represent significant difference at $p < 0.05$.

Table 1
Variance inflation factor (VIF) values for PAR, Ta, VPD, and SWC across different growth stages of kiwifruit under deficit drip irrigation.

Variable	Stage I	Stage II	Stage III	Stage IV	ALL
PAR	1.02	1.02	1.01	1.01	1.01
Ta	9.14	7.94	6.75	2.90	2.09
VPD	9.08	7.78	6.14	2.84	2.08
SWC	1.03	1.04	1.42	1.05	1.00

Notes: I, II, III, and IV refer to bud burst to leafing stage, flowering to fruit set stage, fruit expansion stage, and fruit maturation stage, respectively. PAR: photosynthetically active radiation; Ta: air temperature; VPD: vapor pressure deficit; SWC: soil water content.

One-way ANOVA revealed significant effects of Ta, VPD, and SWC on g_s in all growth stages ($p < 0.05$), while PAR showed a non-significant influence in stage II (Table 2). Across the season, VPD exerted the strongest control on g_s, with effect sizes (η^2) ranging from 0.43 to 0.51, followed by Ta ($\eta^2 = 0.25$–0.50) and SWC ($\eta^2 = 0.17$–0.27). PAR showed only weak effects ($\eta^2 \leq 0.07$).

3.3. Empirical modeling of stomatal conductance

3.3.1. Boundary line analysis of soil water thresholds for maximal stomatal conductance

The relationship between maximum g_s and SWC across different growth stages is illustrated in Fig. 4, and the fitted parameters of soil water response function are summarized in Table 3. Fig. 4 displays the results of the boundary line analysis, where the maximum g_s values were derived as the average of values above the 95th percentile within each SWC class, along with the full dataset of individual measurements for

Table 2
One-way ANOVA results for the effects of environmental variables on stomatal conductance across different growth stages.

Stage	Variation	F-value	p-value	η^2
Stage I	PAR	27.8	2.38×10^{-12}	0.07
	Ta	257.5	5.32×10^{-85}	0.42
	VPD	328.1	6.85×10^{-102}	0.48
	SWC	74.3	4.74×10^{-30}	0.17
Stage II	PAR	1.1	3.37×10^{-1}	0.00
	Ta	353.1	1.77×10^{-107}	0.50
	VPD	375.0	3.38×10^{-112}	0.51
	SWC	113.7	1.30×10^{-43}	0.24
Stage III	PAR	22.1	4.73×10^{-10}	0.06
	Ta	121.7	3.12×10^{-46}	0.25
	VPD	271.0	2.21×10^{-88}	0.43
	SWC	85.3	6.03×10^{-34}	0.19
Stage IV	PAR	15.1	3.79×10^{-07}	0.04
	Ta	150.0	3.68×10^{-55}	0.30
	VPD	229.4	9.80×10^{-78}	0.39
	SWC	133.1	6.93×10^{-50}	0.27

Notes: I, II, III, and IV refer to bud burst to leafing stage, flowering to fruit set stage, fruit expansion stage, and fruit maturation stage, respectively. PAR: photosynthetically active radiation; Ta: air temperature; VPD: vapor pressure deficit; SWC: soil water content.

reference. In the lower range of SWC, maximum g_s increases linearly with increasing SWC. The fitted slopes and SWC_{sc} generally decreased as the growth stages progressed, ranging from 4.50 to 5.07 and 0.139–0.161 $cm^3\ cm^{-3}$, respectively. The slopes and SWC_{sc} in stages I and II were lower than those in stages III and IV, illustrating that g_s was more sensitive to SWC reduction during the early growth period. When SWC exceeded SWC_t, maximum g_s remained relatively stable. Overall,

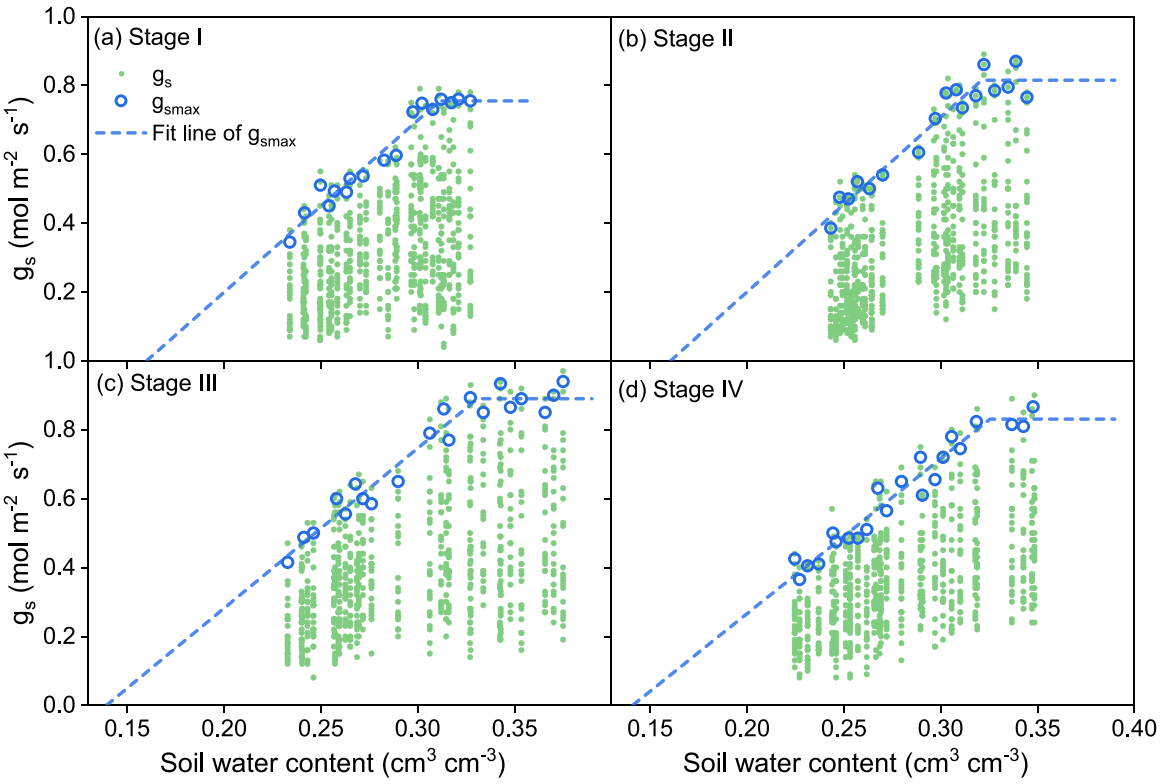

Fig. 4. Relationship between maximum stomatal conductance (g_{smax}) and soil water content of kiwifruit across different growth stages. I, II, III, and IV refer to bud burst to leafing stage, flowering to fruit set stage, fruit expansion stage, and fruit maturation stage, respectively.

Table 3
The fitted parameters of soil water response function for kiwifruit under deficit drip irrigation across different growth stages.

Stage	Slope	SWC_{sc} (cm^3 cm^{-3})	SWC_t (cm^3 cm^{-3})	g_{smax} (mol m^{-2} s^{-1})	R^2
I	4.99	0.160	0.311	0.755	0.96
II	5.07	0.161	0.322	0.815	0.94
III	4.65	0.139	0.331	0.890	0.96
IV	4.50	0.141	0.326	0.831	0.95

Notes: I, II, III, and IV refer to bud burst to leafing stage, flowering to fruit set stage, fruit expansion stage, and fruit maturation stage, respectively. SWC_{sc}: soil water content at which kiwifruit stomata close; SWC_t: soil water content threshold for stomatal conductance reduction; g_{smax}: maximum stomatal conductance.

SWC_t showed an increasing trend as the growth stages progressed, with values of 0.311, 0.322, 0.331, and 0.326 cm^3 cm^{-3} in stages I–IV, respectively. The fitted g_{smax} were 0.755, 0.815, 0.890, 0.831 mol m^{-2} s^{-1} in stages I–IV, respectively.

3.3.2. *Improvement of the Jarvis-type model by incorporating soil water response function*

The validated model parameters of stomatal conductance models for different growth stages are presented in Table 3. Overall, the parameters of the JV1 and JV2 models were more consistent with each other, whereas they differed significantly from those of the JV model, particularly in terms of T_{opt} and g_{smax}. The JV model yielded an unrealistically high T_{opt} in stage III (45.7 °C), whereas the values obtained for JV1 and JV2 were closely aligned with the physiologically reasonable optimum of approximately 30 °C across all stages. Furthermore, T_{opt} tended to be lower during stages I and II and higher during stages III and IV, indicating a dynamic adaptation of stomatal behavior in response to seasonal temperature changes. The calibrated g_{smax} for the JV2 model showed better agreement with the observed g_{smax} compared to those derived from the JV1 model, suggesting that the stage-specific soil water thresholds enhance parameter interpretability Table 4.

In the three Jarvis-type empirical models, both the averaged results (Table 5) and the fold-specific outcomes (Table S1) exhibited consistent performance patterns across growth stages. The JV model showed the lowest accuracy, with R^2 of 0.514–0.649 during training and 0.426–0.622 during testing. Incorporation of soil water response function significantly enhanced model performance. Compared to JV, the JV1 model increased R^2 by 0.144–0.349 and decreased RMSE and MAE by 0.026–0.043 and 0.019–0.035 mol m^{-2} s^{-1}, indicating a substantial regulatory effect of SWC on stomatal dynamics. Further improvements were observed for the JV2 model, which consistently outperformed both JV and JV1 during the testing phase, achieving R^2 between 0.736 and 0.814, RMSE between 0.070 and 0.082 mol m^{-2} s^{-1}, and MAE between

Table 4
Calibrated parameters of Jarvis-type stomatal conductance models for kiwifruit under deficit drip irrigation.

Stage	Model	k_1	$VPD_{0.5}$	k_2	k_3	T_{opt}	g_{smax}
Stage I	JV	250	5.66	2.46	0.0021	28.9	0.77
	JV1	244	5.49	2.54	0.0033	26.1	1.22
	JV2	243	5.66	2.58	0.0035	25.2	0.94
Stage II	JV	179	5.94	3.17	0.0040	28.1	0.73
	JV1	157	3.62	2.94	0.0039	29.8	1.28
	JV2	154	3.58	2.91	0.0038	30.3	0.99
Stage III	JV	199	4.17	2.75	0.0040	45.7	1.78
	JV1	211	3.30	3.81	0.0025	26.8	1.57
	JV2	245	3.77	3.36	0.0039	34.4	1.14
Stage IV	JV	178	3.91	4.22	0.0027	27.4	0.81
	JV1	141	3.66	3.66	0.0032	34.0	1.18
	JV2	149	3.89	3.70	0.0035	33.9	0.92

Notes: I, II, III, and IV refer to bud burst to leafing stage, flowering to fruit set stage, fruit expansion stage, and fruit maturation stage, respectively. k_1, $VPD_{0.5}$, k_2, k_3, T_{opt}, and g_{smax} are parameters for Jarvis-type stomatal conductance models, g_{smax} is maximum stomatal conductance (mol m^{-2} s^{-1}).

Table 5
Performance evaluation of Jarvis-type stomatal conductance model for kiwifruit under deficit drip irrigation.

Stage	Model	Training			Testing		
		R^2	RMSE (mol m^{-2} s^{-1})	MAE (mol m^{-2} s^{-1})	R^2	RMSE (mol m^{-2} s^{-1})	MAE (mol m^{-2} s^{-1})
Stage I	JV	0.617	0.102	0.080	0.581	0.108	0.084
	JV1	**0.761**	**0.081**	**0.064**	0.725	0.082	0.066
	JV2	0.762	0.084	0.066	**0.736**	**0.082**	**0.065**
Stage II	JV	0.649	0.106	0.082	0.622	0.118	0.090
	JV1	0.833	0.073	0.060	0.803	0.079	0.064
	JV2	**0.837**	**0.072**	**0.060**	**0.814**	**0.076**	**0.063**
Stage III	JV	0.590	0.119	0.095	0.558	0.124	0.100
	JV1	0.787	0.087	0.070	0.793	0.085	0.069
	JV2	**0.812**	**0.081**	**0.067**	**0.813**	**0.079**	**0.066**
Stage IV	JV	0.514	0.108	0.084	0.426	0.117	0.093
	JV1	0.780	0.073	0.058	0.775	0.074	0.058
	JV2	**0.799**	**0.069**	**0.057**	**0.792**	**0.070**	**0.057**

Notes: I, II, III, and IV refer to bud burst to leafing stage, flowering to fruit set stage, fruit expansion stage, and fruit maturation stage, respectively.

0.063 and 0.066 mol m^{-2} s^{-1}, reflecting the effectiveness of incorporating stage-specific soil water thresholds. The fold-specific cross-validation results provided additional support for these findings. Across the three year-based folds (Table S1), the JV2 model maintained the highest R^2 and lowest RMSE and MAE among the three empirical models. Although some interannual variability was observed, the fluctuations in JV2 performance were relatively small, indicating that the improved soil water response function enhances model robustness and generalization across different years Tables 6 and 7.

Violin plots showing the measured g_s and the simulated values from the JV, JV1, and JV2 models across different growth stages are presented in Fig. 5. The IQR of measured g_s in stages I–IV were 0.18–0.43, 0.18–0.44, 0.26–0.51, and 0.25–0.45 mol m^{-2} s^{-1}, respectively. Across all stages, the JV model produced notably narrower distributions compared to the observed measurements. The IQRs for JV were 0.194–0.381, 0.197–0.386, 0.282–0.493, and 0.275–0.419 mol m^{-2} s^{-1} for stages I–IV, respectively, indicating a systematic underestimation of high g_s values and an overestimation of low g_s values. In contrast, the simulated g_s distributions from JV1 and JV2 more closely resembled the measured patterns in both spread and density. The two models exhibited similar performance; however, JV2 showed slightly better agreement with observations. The IQRs of JV2 were 0.193–0.425, 0.179–0.387, 0.271–0.502, and 0.251–0.440 mol m^{-2} s^{-1} for stages I–IV, respectively.

Table 6
Performance evaluation of machine learning models for predicting kiwifruit stomatal conductance using PAR, Ta, and VPD as input variables.

Stage	Model	Training			Testing		
		R^2	RMSE (mol m^{-2} s^{-1})	MAE (mol m^{-2} s^{-1})	R^2	RMSE (mol m^{-2} s^{-1})	MAE (mol m^{-2} s^{-1})
Stage I	XGBoost	0.769	0.078	0.062	0.628	0.097	0.074
	LightGBM	0.837	0.066	0.051	0.650	0.095	0.072
	CatBoost	**0.870**	**0.059**	**0.049**	**0.724**	**0.084**	**0.066**
	SVR	0.405	0.129	0.099	0.354	0.142	0.113
	LR	0.589	0.104	0.082	0.515	0.111	0.088
Stage II	XGBoost	0.817	0.075	0.059	0.630	0.108	0.084
	LightGBM	0.861	0.065	0.052	0.625	0.109	0.083
	CatBoost	**0.887**	**0.059**	**0.047**	**0.712**	**0.095**	**0.080**
	SVR	0.427	0.149	0.110	0.285	0.158	0.119
	LR	0.577	0.114	0.090	0.525	0.119	0.095
Stage III	XGBoost	0.769	0.088	0.071	0.566	0.120	0.095
	LightGBM	0.836	0.074	0.059	0.581	0.118	0.095
	CatBoost	**0.869**	**0.067**	**0.055**	**0.660**	**0.106**	**0.089**
	SVR	0.181	0.167	0.127	0.129	0.173	0.134
	LR	0.542	0.124	0.097	0.500	0.131	0.102
Stage IV	XGBoost	0.756	0.076	0.059	0.500	0.108	0.086
	LightGBM	0.840	0.061	0.048	0.496	0.107	0.084
	CatBoost	**0.866**	**0.057**	**0.044**	**0.576**	**0.099**	**0.079**
	SVR	0.259	0.133	0.101	0.173	0.142	0.109
	LR	0.503	0.108	0.084	0.387	0.118	0.093

Notes: I, II, III, and IV refer to bud burst to leafing stage, flowering to fruit set stage, fruit expansion stage, and fruit maturation stage, respectively.

Table 7
Performance evaluation of machine learning models for predicting kiwifruit stomatal conductance using PAR, Ta, VPD, and SWC as input variables.

Stage	Model	Training			Testing		
		R^2	RMSE (mol m^{-2} s^{-1})	MAE (mol m^{-2} s^{-1})	R^2	RMSE (mol m^{-2} s^{-1})	MAE (mol m^{-2} s^{-1})
Stage I	XGBoost	0.814	0.070	0.055	0.768	0.076	0.060
	LightGBM	0.871	0.058	0.046	0.765	0.076	0.058
	CatBoost	**0.887**	**0.055**	**0.044**	**0.839**	**0.065**	**0.057**
	SVR	0.519	0.118	0.091	0.466	0.130	0.104
	LR	0.604	0.099	0.069	0.677	0.093	0.081
Stage II	XGBoost	0.871	0.063	0.052	0.791	0.081	0.066
	LightGBM	0.901	0.055	0.045	0.791	0.081	0.065
	CatBoost	**0.916**	**0.051**	**0.042**	**0.830**	**0.073**	**0.063**
	SVR	0.525	0.129	0.095	0.494	0.136	0.102
	LR	0.796	0.079	0.064	0.779	0.082	0.066
Stage III	XGBoost	0.860	0.069	0.056	0.790	0.083	0.067
	LightGBM	0.896	0.059	0.048	0.803	0.081	0.065
	CatBoost	**0.910**	**0.055**	**0.046**	**0.826**	**0.076**	**0.064**
	SVR	0.395	0.146	0.113	0.327	0.153	0.120
	LR	0.768	0.088	0.071	0.770	0.088	0.071
Stage IV	XGBoost	0.846	0.060	0.047	0.768	0.073	0.057
	LightGBM	0.886	0.052	0.041	0.775	0.071	0.056
	CatBoost	**0.907**	**0.047**	**0.037**	**0.815**	**0.065**	**0.054**
	SVR	0.508	0.112	0.085	0.437	0.117	0.091
	LR	0.717	0.088	0.071	0.732	0.078	0.062

Notes: I, II, III, and IV refer to bud burst to leafing stage, flowering to fruit set stage, fruit expansion stage, and fruit maturation stage, respectively.

The relative residuals of empirical stomatal conductance models under different SWC conditions are illustrated in Fig. 6. It can be seen that the JV model produced the largest relative residuals across all stages, with a tendency to overestimate g_s under low SWC conditions and to underestimate it under high SWC conditions. In contrast, the JV1 and JV2 models demonstrated consistently stable and comparable performance across all SWC levels, indicating greater reliability in their estimations. Compared to the JV1 model, the JV2 model exhibited more tightly clustered relative residuals that were closer to zero under extreme SWC conditions, particularly at FC levels ranging from 60 to 65 % and 85–95 % during stages I, II, and IV, and from 90 to 100 % during stage III.

Overall, the saturation constraint implemented in JV2 effectively reflects the physiological phenomenon that stomatal opening no longer increases once a critical soil water threshold is reached, thereby enhancing both the biological plausibility and predictive stability of the model. Furthermore, the performance comparison showed that incorporating both the magnitude and saturation characteristics of SWC response is crucial for reliably modeling g_s under varying SWC scenarios.

3.4. Modeling and interpretation of stomatal conductance using machine learning

3.4.1. Estimation of stomatal conductance using machine learning algorithms

The performance of five machine learning models (XGBoost, LightGBM, CatBoost, SVR, and LR) in simulating g_s was evaluated using two sets of input variables: PAR, Ta, and VPD (Table 6 and S2), and PAR, Ta, VPD, and SWC (Table 7 and S3). When PAR, Ta, and VPD were used as input features, testing R^2 values for all models were notably lower

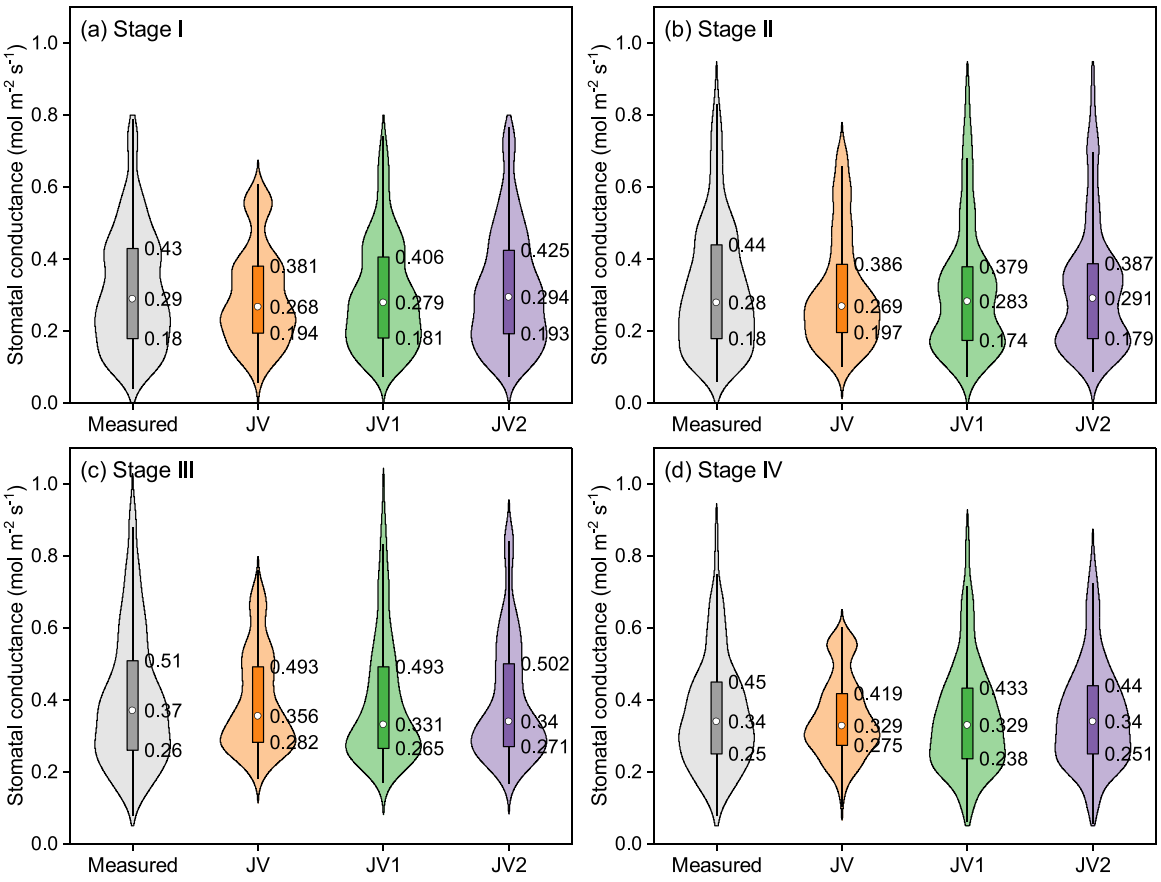

Fig. 5. Violin plots showing the measured stomatal conductance and the simulated values from the JV, JV1, and JV2 models across different growth stages.

than training R^2, indicating varying degrees of overfitting. Tree-based ensemble models significantly outperformed SVR and LR across all growth stages. Among these models, CatBoost exhibited the highest predictive accuracy, achieving testing R^2 ranging from 0.576 to 0.724, RMSE between 0.084 and 0.106 mol m^{-2} s^{-1}, and MAE between 0.066 and 0.089 mol m^{-2} s^{-1}. LightGBM performed comparably to CatBoost during the training phase; however, its testing accuracy declined notably, reflecting evident overfitting and limited generalization capability under constrained input conditions. XGBoost yielded moderate performance, whereas SVR and LR displayed relatively poor performance, characterized by low testing R^2 values and high RMSE and MAE, suggesting potential underfitting.

When PAR, Ta, VPD, and SWC were used as input variables, CatBoost consistently demonstrated superior overall performance in estimating g_s, with minimal difference between training and testing results, indicating strong generalization capability (Table 7 and S3). It achieved testing R^2 ranging from 0.815 to 0.839, RMSE between 0.065 and 0.076 mol m^{-2} s^{-1}, and MAE between 0.054 and 0.064 mol m^{-2} s^{-1}. LightGBM exhibited robust performance during the training phase but experienced a notable decline in testing accuracy, which occasionally fell below that of XGBoost, further illustrating issues of overfitting and limited generalizability. SVR consistently displayed poor and comparable accuracy in both training and testing phases, reflecting typical underfitting behavior.

Across the three year-based folds, CatBoost consistently achieved the highest testing R^2 and the lowest testing RMSE and MAE among all machine learning models (Table S3). The differences between its training and testing R^2 below 0.15 in each fold, and its fold-to-fold variation in both R^2 and RMSE was minimal. These results demonstrate that CatBoost delivered the most stable and accurate predictive performance over different years.

Incorporating SWC into the models enhanced the goodness-of-fit and reduced prediction errors across all growth stages and machine learning algorithms (Fig. 7). CatBoost, which already achieved high accuracy with three input variables (PAR, Ta, VPD), showed further significant improvements after adding SWC, with testing R^2 increasing by 0.115–0.239 and RMSE and MAE reduced by 0.019–0.035 and 0.010–0.025 mol m^{-2} s^{-1}, respectively. LR exhibited the greatest relative improvement in R^2; however, its overall accuracy remained notably lower compared to ensemble learning models. The most substantial improvements across all models were observed during stages III and IV, with marked reductions in RMSE and MAE.

Violin plots comparing the measured g_s with simulated values from five machine learning models using PAR, Ta, VPD, and SWC as input variables across different growth stages are shown in Fig. 8. The distribution characteristics revealed clear performance differences among the models. SVR produced a substantially narrower IQR than the measured g_s and exhibited a markedly different density pattern. LR produced IQR similar to the measurements, but its density patterns differed substantially, indicating poor reconstruction of the underlying distribution. In contrast, the three tree-based ensemble models (XGBoost, LightGBM, and CatBoost) yielded distributions more similar to the observed g_s in both IQR and density shape. Among them, CatBoost provided the closest match to the measured distributions, with IQRs of 0.211–0.424, 0.184–0.408, 0.287–0.520, and 0.259–0.442 mol m^{-2} s^{-1} for stages I–IV, respectively. These results highlight that CatBoost most accurately captures both the magnitude and distributional characteristics of g_s.

Overall, the incorporation of SWC substantially enhanced the accuracy of machine learning models in predicting g_s. Regardless of input variable combinations, ensemble learning models consistently outperformed SVR and LR, and CatBoost exhibited the highest accuracy,

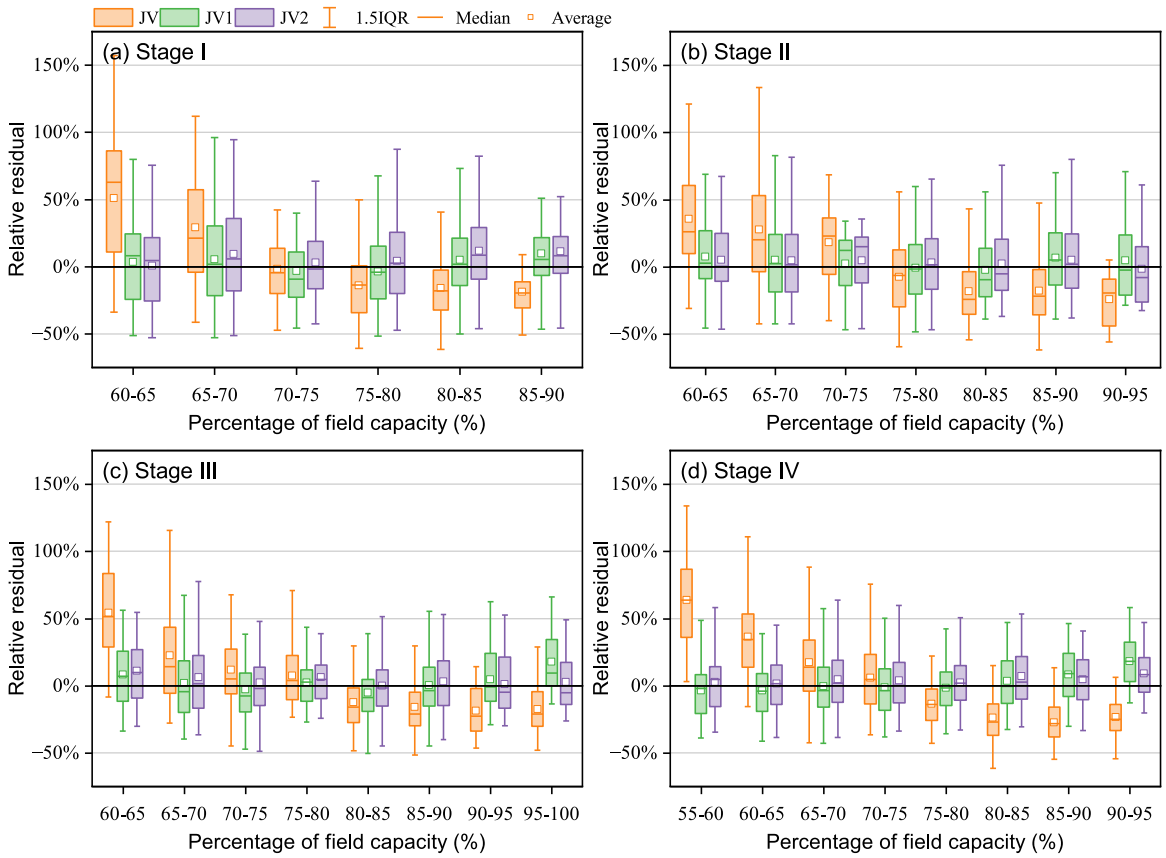

Fig. 6. Relative residuals of Jarvis-type models in estimating stomatal conductance under different soil water content conditions. I, II, III, and IV refer to bud burst to leafing stage, flowering to fruit set stage, fruit expansion stage, and fruit maturation stage, respectively.

stability, and generalization capability across all growth stages.

3.4.2. *Quantification of variable contributions*

To enhance the interpretation of model outputs and assess the key driving factors influencing g_s variation, SHAP analysis was conducted using the top-performing machine learning model, CatBoost, under two input scenarios (Figs. 9a and b). When PAR, VPD, and Ta were used as input variables, VPD consistently demonstrated the highest mean SHAP values across all stages, underscoring its predominant influence in regulating g_s. Specifically, the mean SHAP value of VPD during stages I–IV was 0.084, 0.081, 0.103, and 0.054, respectively. In stages II and IV, Ta ranked second following VPD, with mean SHAP values of 0.053 and 0.040, respectively. Conversely, PAR exhibited relatively greater importance compared to Ta in stages I and III.

When SWC was included as an input variable, VPD remained the most influential factor (Figs. 9c and 9d). However, the differences between VPD and SWC were relatively minor. Specifically, the mean SHAP values of VPD across stages I to IV were 0.065, 0.064, 0.079, and 0.063, respectively, while the corresponding mean SHAP values for SWC were 0.050, 0.062, 0.073, and 0.061. In stages II and IV, the mean SHAP values of SWC approached those of VPD. The contributions of Ta and PAR remained relatively minor, with average SHAP values generally below 0.05.

These results suggest that VPD is the primary factor influencing g_s variability under both input configurations. Incorporating soil moisture into the model improves its interpretability by accounting for the effects of water stress. The comparable SHAP value magnitudes of VPD and SWC in later growth stages underscore the complementary roles of atmospheric transpiration demand and soil water availability in regulating kiwifruit stomatal behavior.

The PDPs illustrate the marginal effects of the four environmental variables on g_s across the four growth stages (Fig. 10). For PAR, a rapid increase in g_s was observed below approximately 700 μmol m^{-2} s^{-1} during stages II–IV, followed by a gradual plateau during stages II–IV. Ta exhibited a typical asymmetric unimodal response. In stage I, g_s peaked at around 25 °C, while in stages II–IV, the optimum temperature shifted upward to approximately 32–36 °C. VPD exerted a strong negative effect on g_s across all stages. Once VPD exceeded roughly 1.5–2.0 kPa, g_s declined sharply. SWC consistently showed a positive marginal effect across all growth stages. The most pronounced increase in g_s occurred as SWC increased from dry conditions toward field capacity, with the response diminishing under wetter soil conditions.

4. Discussion

4.1. *Responses of kiwifruit stomatal conductance to deficit irrigation*

In the present study, deficit irrigation significantly decreased gs of kiwifruit at different growth stages (Fig. 3), which aligns with previous findings by Mills et al. (2009) and Rogiers et al. (2012). Water deficit triggered drought response mechanisms by reducing soil water availability. To minimize water loss, plants regulate multiple signaling pathways and close their stomata under water-limited conditions, representing a self-protective adaptive strategy (Rodriguez-Dominguez and Brodribb, 2020; Li and Liu, 2022a).

Importantly, the impact of deficit irrigation on g_s was found to vary across growth stages. The stage-specific sensitivity of g_s to SWC was quantified through two complementary approaches. Under near-ideal conditions (as revealed by boundary line analysis, Fig. 4 and Table 1), the intrinsic sensitivity, represented by the slope of the g_{smax}-SWC relationship, was highest in stage I (4.99) and II (5.07), demonstrating the greatest physiological responsiveness to soil moisture during early

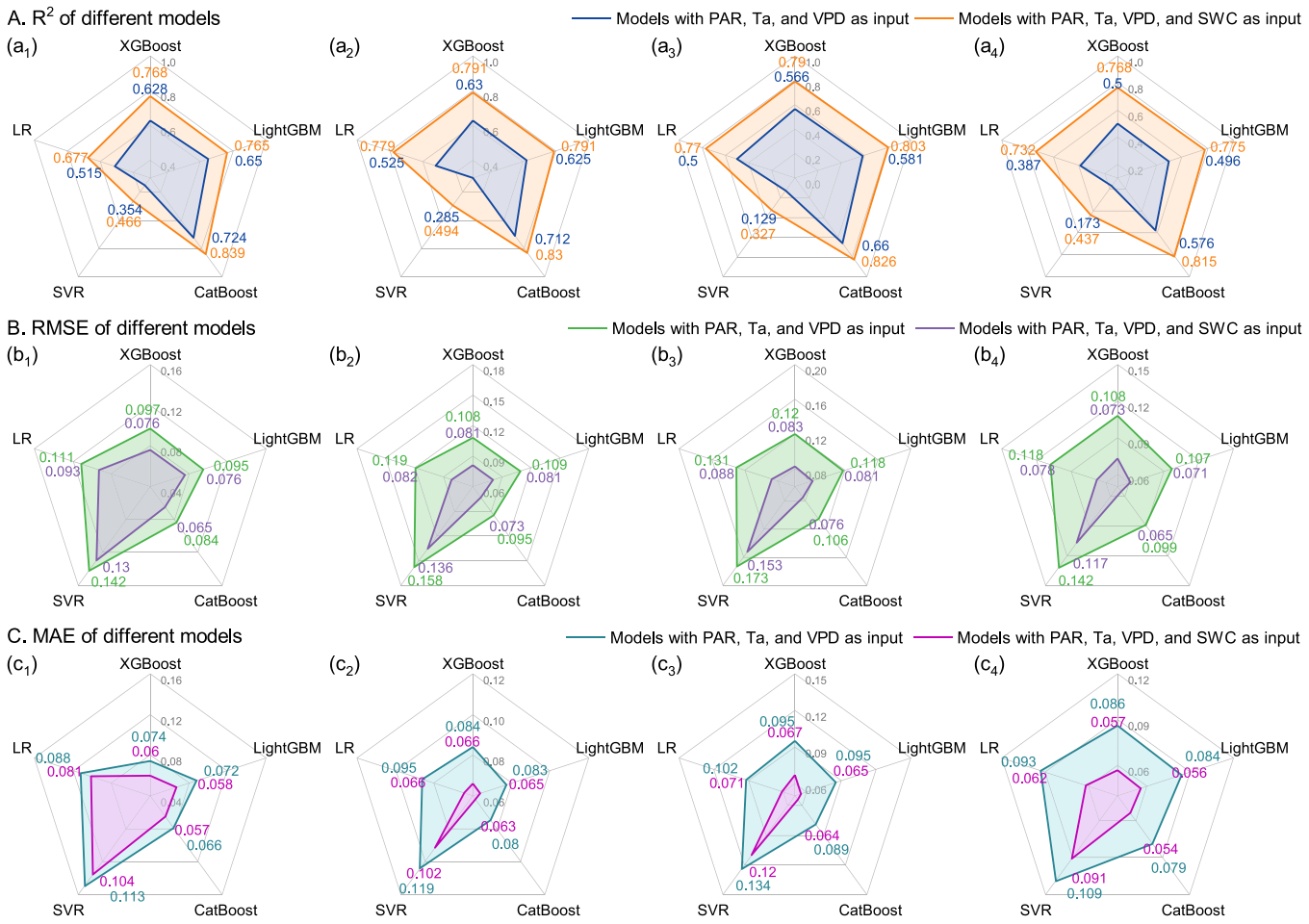

Fig. 7. Radar plots comparing model performance (R^2, RMSE, and MAE) of five machine learning models (XGBoost, LightGBM, CatBoost, SVR, and LR) in estimating stomatal conductance using different input variable combinations. I, II, III, and IV refer to bud burst to leafing stage, flowering to fruit set stage, fruit expansion stage, and fruit maturation stage, respectively.

vegetative growth. This may be attributed to the greater sensitivity of immature leaves to water stress (Funk et al., 2021). In contrast, under actual field conditions where multiple environmental factors interact (as quantified by ANOVA, Table 2), the relative importance of SWC (η^2) in explaining g_s variation showed a different pattern: it was most pronounced in stage II (0.24) and stage IV (0.27). This indicates that while the leaf's inherent physiological responsiveness to soil moisture is strongest early in the season, the actual impact of SWC on stomatal behavior is most ecologically significant during the critical fruit set (stage II) and maturation (stage IV) periods. The particularly high sensitivity observed in stage II through both metrics underscores its dual significance as a period of both high physiological sensitivity and substantial ecological impact.

Although a positive correlation between SWC and g_s is well documented (Carminati and Javaux, 2020; Lamptey et al., 2020), this relationship is not strictly linear. Previous studies have identified a stable phase of g_s during the early stages of water deficit, where g_s remains relatively constant despite decreasing SWC (Qi et al., 2023; Wang et al., 2018). Similar patterns have been reported in tomatoes and grasses, with reductions in g_s occurring only after SWC drops below a specific threshold, typically within the range of 80–90 % of FC (Li and Liu, 2022; Huang et al., 2020). Comparable thresholds were identified for kiwifruit in the present study, with g_s decline occurring at SWC values between 0.311 and 0.331 cm^3 cm^{-3} across different stages (Table 1). These thresholds represent the upper limits beyond which further increases in SWC do not enhance g_s but may instead contribute to excessive water loss. The observed variability in SWC thresholds can be attributed to dynamic interactions between plant physiological responses and environmental conditions, underscoring the complex and non-linear nature of stomatal regulation under combined environmental influences.

4.2. *Enhancement of Jarvis-type stomatal conductance models by incorporating soil water response functions*

The original Jarvis model assumes that g_s is independently regulated by environmental variables such as PAR, Ta, and VPD. It has been shown to perform well under well-watered conditions (Wang et al., 2018). However, this type of model often fails to adequately account for the influence of soil water availability in water-limited scenarios. In the present study, the JV model showed low estimation accuracy across different stages (Table 2). Furthermore, the model displayed systematic residual biases, overestimating g_s at low SWC and underestimating it at high SWC (Fig. 6). These results align with those reported by Wang et al. (2018) and Li et al. (2023), further indicating the limitations of the JV model under drought conditions.

To address the limitations, a classical soil water response function f_1(SWC) was integrated into the Jarvis model, thereby significantly enhancing the accuracy of g_s estimation under varying SWC conditions. In this study, the JV1 model incorporating f_1(SWC) exhibited markedly improved performance in estimating g_s across all growth stages. However, f_1(SWC) assumes a linear decline of g_s between field capacity and the permanent wilting point, which may lead to inaccuracies (Qi et al., 2023; Wang et al., 2018). While such linear formulations represent an important step forward, they fail to capture the nonlinear and saturating

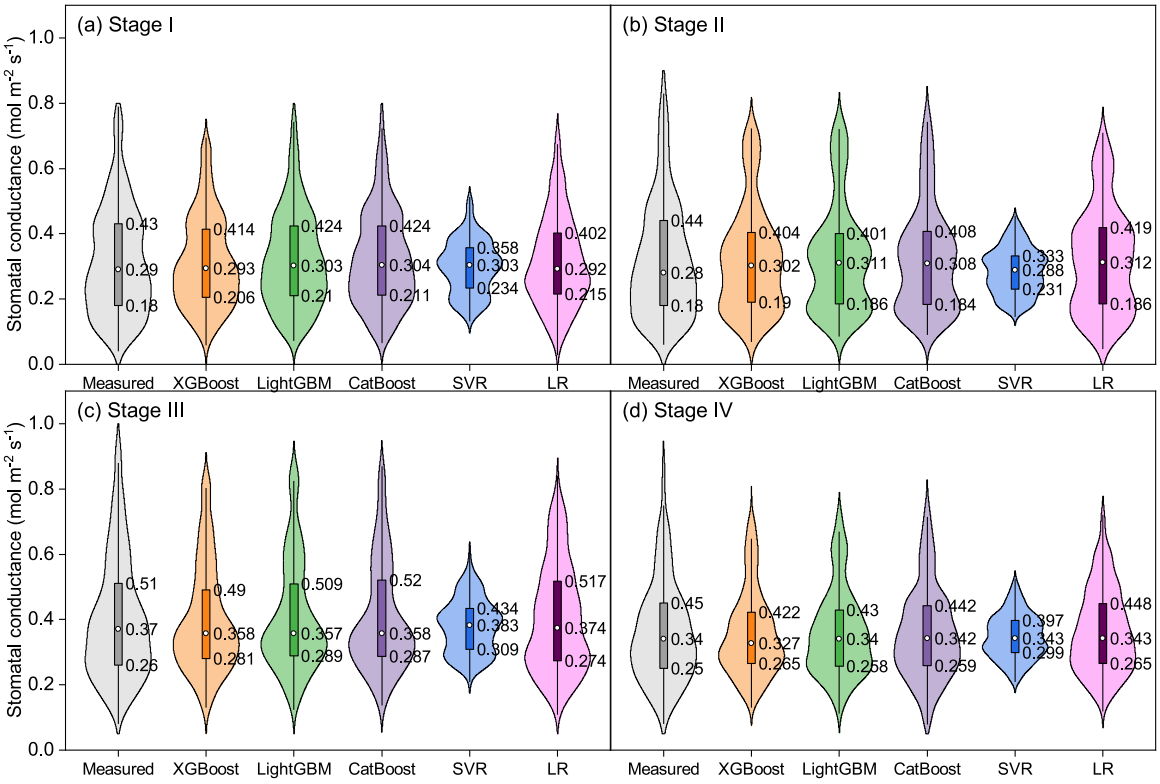

Fig. 8. Violin plots showing the measured stomatal conductance and the simulated values from five machine learning models (XGBoost, LightGBM, CatBoost, SVR, and LR) using PAR, Ta, VPD, and SWC as input variables across different growth stages.

nature of the gs–SWC relationship, particularly under extreme conditions. In this study, a novel soil water response function f_2(SWC) was proposed. Its core advancement is the incorporation of a nonlinear saturation constraint defined by stage-specific thresholds. By better capturing the saturation behavior of g_s, the JV2 model further improved g_s estimation accuracy. As a result, under extreme SWC conditions, the JV2 model exhibited more tightly clustered and near-zero relative residuals compared to the JV1 model (Fig. 6), indicating enhanced generalization performance.

4.3. Superiority of machine learning models in stomatal conductance prediction

In this study, ensemble learning models based on gradient boosting decision trees (XGBoost, CatBoost, and LightGBM) demonstrated superior performance over traditional machine learning algorithms (SVR and LR) in simulating g_s. These models are capable of capturing complex nonlinear relationships and interaction effects among variables, thereby making them particularly suitable for eco-physiological prediction tasks under field conditions (Alizamir et al., 2024). In contrast, SVR exhibited limitations in modeling the high-dimensional nonlinear patterns involved in stomatal regulation, which may be attributed to the limited expressiveness of its kernel functions and its sensitivity to sparse data (Ara et al., 2022; Sekeroglu et al., 2022). LR, constrained by its simplistic linear assumptions (Sekeroglu et al., 2022), also failed to adequately capture the complexity of stomatal responses. Overall, these findings underscore the substantial advantages of gradient boosting-based ensemble models over conventional machine learning approaches for g_s prediction.

Among the ensemble models, CatBoost consistently demonstrated the highest prediction accuracy and superior generalization performance across all growth stages. This can be attributed to its ordered boosting algorithm and integrated mechanisms for managing feature distributions, which effectively mitigate overfitting and enhance model robustness under conditions of limited or imbalanced input data in g_s simulation (Alizamir et al., 2024). In contrast, although XGBoost exhibited strong performance during the training phase, it showed a noticeable decline in accuracy during testing, indicating limited generalization and a tendency toward overfitting. This discrepancy may stem from the pronounced diurnal variation in g_s, as stomata tend to open rapidly under favorable morning conditions, leading to an uneven concentration of high-g_s samples in the dataset. These nonlinear and dynamic patterns may intensify XGBoost's tendency toward biased feature partitioning during training, ultimately compromising its predictive performance (Niazkar et al., 2024).

Compared to empirical models, machine learning algorithms achieved higher accuracy in predicting g_s, which aligns with findings in farmland (Houshmandfar et al., 2021) and forest ecosystems (Saunders et al., 2021). The empirical model JV2 achieved reasonable estimation performance while maintaining interpretable parameter structures. Nevertheless, CatBoost surpassed the performance of the JV2 model across all growth stages, achieving testing R^2 values higher than JV2's maximum of 0.815, despite lacking mechanistic constraints. This superiority stems from its ability to automatically learn complex interactions among input variables, which empirical models typically fail to capture.

4.4. Feature attribution and physiological implications unveiled through SHAP and partial dependence analysis

To further elucidate the behavior of machine learning models and the underlying physiological mechanisms governing g_s, SHAP analysis coupled with PDPs was performed based on the CatBoost algorithm. This integrated approach enabled the quantification of the relative influence of multiple driving factors and the visualization of their marginal effects on g_s, facilitating a stage-specific interpretation of g_s regulation.

Across all growth stages, VPD emerged as the most consistently influential predictor, confirming its predominant influence on the variation in g_s of kiwifruit under varying SWC conditions (Fig. 9). This

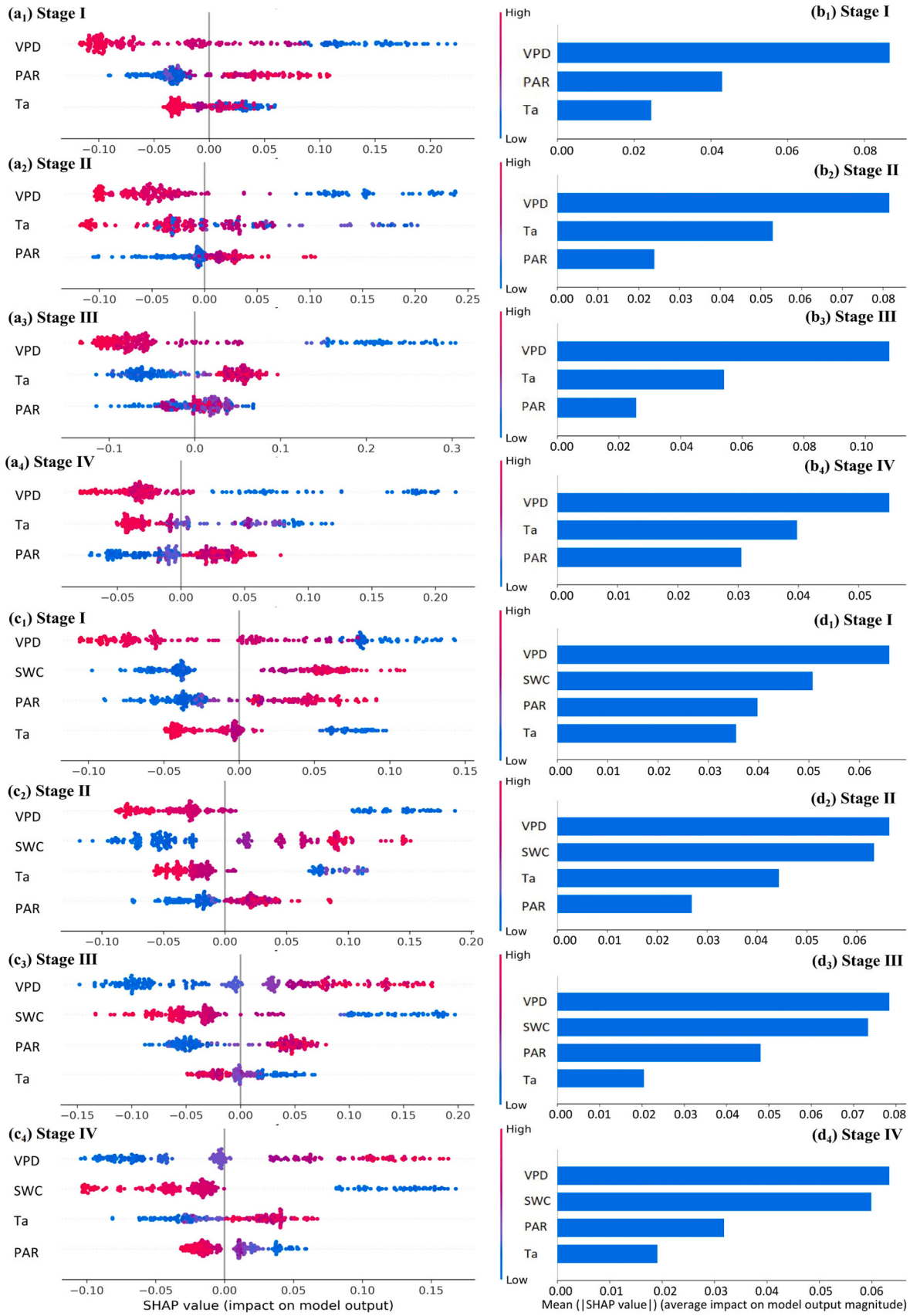

Fig. 9. SHAP-based interpretation of variable importance in CatBoost predictions of stomatal conductance. Subplots a and b represent models using photosynthetically active radiation (PAR), air temperature (Ta), and vapor pressure deficit (VPD) as inputs; c and d represent models that additionally incorporate soil water content (SWC). Subplots a and c showed SHAP summary plots; b and d display mean absolute SHAP values.

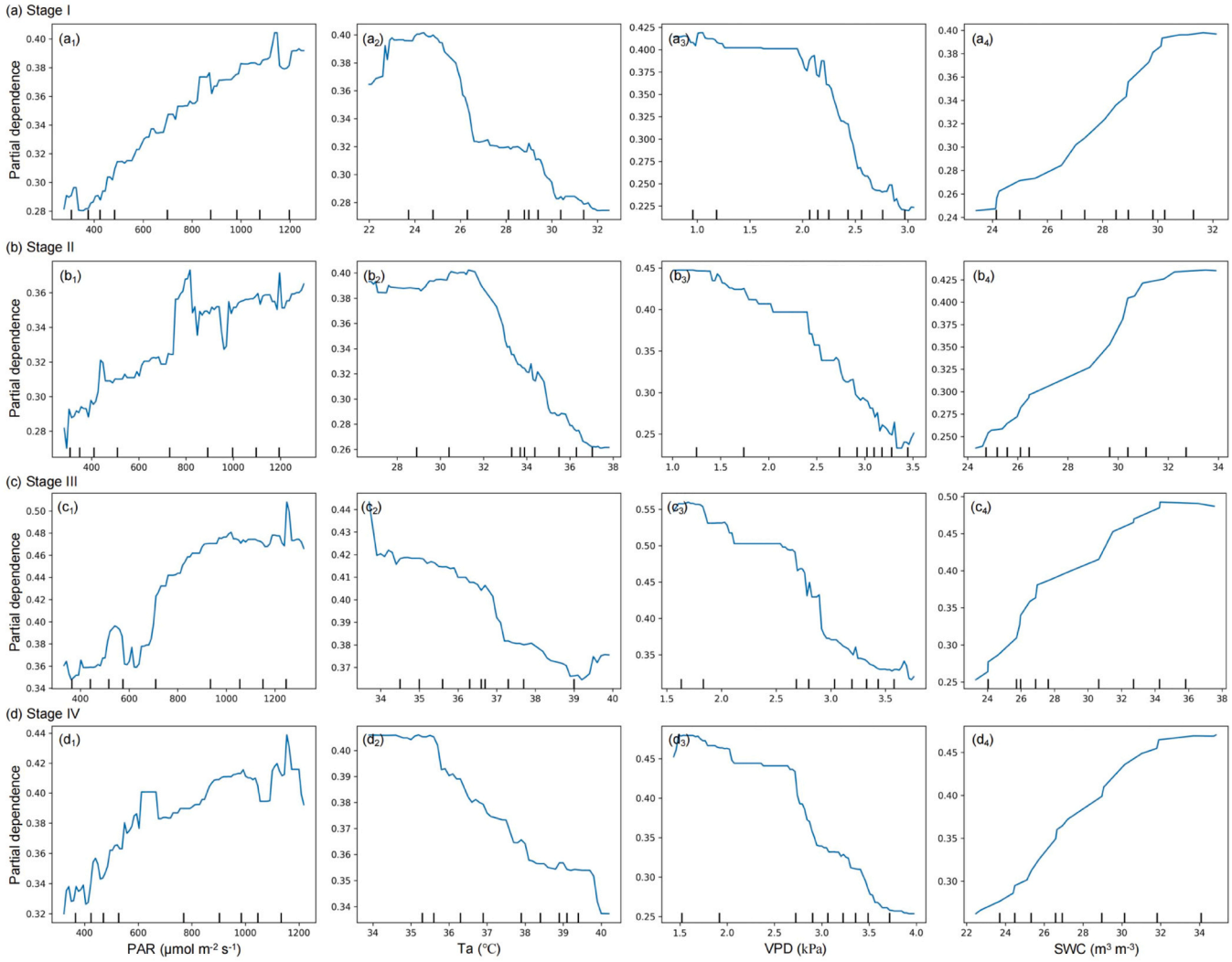

Fig. 10. Partial dependence plots showing the marginal effects of PAR, Ta, VPD, and SWC on stomatal conductance predicted by the CatBoost model across different growth stages of kiwifruit.

finding aligns with preliminary ANOVA results, which similarly identified VPD as the factor with the largest effect size (η^2). The dominance of VPD aligns with well-established physiological principles indicating that VPD directly influences transpiration demand and stomatal aperture (Grossiord et al., 2020; Gaur and Drewry, 2024). As a key indicator of atmospheric evaporative demand, elevated VPD intensifies the water vapor gradient from the leaf to the air, thereby accelerating transpiration rates (Jalakas et al., 2021). To prevent excessive water loss and mitigate the risk of hydraulic failure, plants actively regulate stomatal aperture by closing stomata under high VPD, representing a crucial water-conserving mechanism (Buckley, 2019; Li and Liu, 2022a). This robust regulatory mechanism is clearly illustrated in the PDPs (Fig. 10), where g_s exhibits a pronounced decline once VPD surpasses a threshold of approximately 1.5–2.0 kPa across all stages, providing visual confirmation of the protective stomatal response.

The SHAP values of SWC were comparable to or slightly lower than those of VPD, confirming its substantial influence in regulating g_s under water-limited conditions (Qi et al., 2023; Li et al., 2023). Notably, the co-dominance of VPD and SWC suggests a key interaction between atmospheric evaporative demand and soil water availability. This aligns with the physiological principle that stomatal sensitivity to VPD is modulated by soil moisture status (Grossiord et al., 2020). The PDPs for SWC consistently showed a positive marginal effect, with g_s increasing most rapidly as SWC rose from dry levels toward a threshold value, followed by a gradual plateau under wetter soil conditions (Fig. 10). This saturation pattern underscores the nonlinear relationship between g_s and SWC. Furthermore, the significant improvement in machine learning model performance upon incorporating SWC further substantiates its regulatory importance. The stage-dependent discrepancy between the intrinsic sensitivity to SWC (as shown by boundary line slopes) and its explanatory power in the field observations (ANOVA η^2) may reflect this dynamic interplay, where the dominance of VPD during certain stages can mask the expression of SWC's influence.

In contrast, PAR exhibited lower SHAP values, indicating a relatively smaller influence on the model output. The PDPs for PAR revealed an initial sharp increase in g_s at low light intensities, followed by a plateau, reflecting the typical stomatal response to light saturation (Lawson and Vialet-Chabrand, 2019). Although increasing PAR generally enhances photosynthesis, reduces intercellular CO_2 concentration and promotes stomatal opening to facilitate carbon uptake (Lawson and Vialet-Chabrand, 2019; Driesen et al., 2020), this effect may plateau or decrease when PAR reaches light saturation levels, raises leaf temperature, or increases VPD, potentially stabilizing or reducing g_s (Li et al., 2022b). Ta demonstrated the smallest overall contribution, as its impact on g_s was primarily indirect, mediated largely through its effect on VPD (Whitehead, 1998). While temperature has the potential to affect enzymatic activity and membrane fluidity, its direct impact on g_s was relatively minor in this study. This may result from the complex

interplay between positive and negative feedback mechanisms in stomatal regulation under varying environmental conditions.

Overall, the SHAP and PDPs results collectively indicated that g_s of kiwifruit is regulated by both atmospheric and soil water availability. VPD emerged as the dominant factor, followed by SWC. Ta and PAR exhibited more limited and context-dependent influences. This multifactorial regulation underscores the complexity of stomatal behavior and highlights the value of explainable machine learning approaches in elucidating the dynamic importance of environmental variables.

4.5. Applicability, limitations, and future directions

This study developed both Jarvis-type empirical models and machine learning models to simulate g_s of kiwifruit under varying SWC conditions. The improved JV2 model achieved acceptable estimation accuracy while preserving structural transparency and physiological interpretability. In comparison, CatBoost exhibited superior prediction performance and adaptability across different growth stages. These results suggest that, in orchards where reliable environmental and soil moisture data are available, both modeling approaches can effectively support accurate estimation and regulation of g_s in kiwifruit production. Specifically, the estimated g_s values can be benchmarked against g_{smax} to assess plant water status, or coupled with evapotranspiration models to improve the accuracy of water flux simulations. Furthermore, the stage-specific SWC thresholds identified in this study offer directly applicable irrigation triggers when compared with real-time SWC data. This multifaceted approach provides reliable physiological references for optimizing irrigation schedules, advancing beyond traditional methods based solely on SWC monitoring.

However, the models were developed using data from a single site and cultivar, which may limit their immediate applicability to other regions or kiwifruit varieties without appropriate recalibration. Moreover, although the machine learning model demonstrated strong performance, it depends on high-quality, multivariate input data that may not be consistently available in typical production environments. Additionally, the current models considered only environmental factors and SWC, neglecting potential root-zone dynamics, plant hydraulic traits, and long-term inter-seasonal feedbacks.

Future research should prioritize several key directions to advance the findings of this study. First, expanding datasets across multiple years, diverse cultivars, and varied agroecological zones is essential for improving model robustness and transferability. Second, incorporating plant hydraulic traits and other physiological variables could significantly enhance the mechanistic basis of g_s models. Third, developing hybrid modeling frameworks that integrate the interpretability of mechanistic models with the predictive power of data-driven approaches would leverage the strengths of both methodologies (Elshaarawy et al., 2024). Additionally, implementing comprehensive uncertainty quantification and resilience analysis would provide deeper insights into model stability under varying environmental conditions. Finally, designing user-friendly software tools would facilitate the practical adoption of these models among agricultural practitioners. Collectively, these efforts will establish a more robust foundation for g_s modeling and enable more accurate simulations in land surface and crop modeling systems.

5. Conclusion

This study investigated the stage-specific response of kiwifruit g_s to deficit drip irrigation and evaluated the performance of improved empirical and machine learning models in simulating g_s under varying soil water conditions. The key conclusions are summarized as follows:

(1) Deficit irrigation significantly reduced g_s of kiwifruit, with g_s displaying distinct stage-specific responses to SWC across different growth stages. During stages I and II, g_s demonstrated higher sensitivity to reductions in SWC. The SWC thresholds triggering g_s reductions were 0.311, 0.322, 0.331, and 0.326 cm^3 cm^{-3} for stages I–IV, respectively.

(2) Incorporating soil water response functions into the Jarvis-type model substantially improved its performance in predicting g_s. The JV2 model, which introduced a nonlinear saturation constraint, achieved the highest prediction accuracy and effectively reduced systematic bias, especially under extreme SWC conditions.

(3) Among the five evaluated machine learning models, CatBoost consistently outperformed both empirical models and other machine learning models, achieving the highest R^2 and lowest RMSE across all stages. SHAP analysis and PDPs further revealed that VPD was the most influential driver of g_s variation, followed by SWC, while PAR and Ta exhibited moderate to limited contributions.

Overall, the improved JV2 model significantly enhanced g_s estimation, while CatBoost demonstrated superior predictive performance, offering enhanced interpretability through SHAP analysis and PDPs. These findings provide a robust foundation for accurately modeling and regulating kiwifruit g_s under water-limited conditions.

CRediT authorship contribution statement

Ningbo Cui: Writing – review & editing, Validation, Investigation, Funding acquisition. **Shunsheng Zheng:** Writing – review & editing, Writing – original draft, Methodology, Investigation, Formal analysis. **Shouzheng Jiang:** Investigation, Funding acquisition. **Quanshan Liu:** Writing – review & editing, Validation, Methodology. **Xiaoxian Zhang:** Writing – review & editing, Methodology. **Daozhi Gong:** Writing – review & editing.

Declaration of Competing Interest

The authors declare that they have no known competing financial interests or personal relationships that could have appeared to influence the work reported in this paper.

Acknowledgments

This work was supported by the National Natural Science Foundation of China (51922072, 52109060, 52279041), the Science and Technology Program of Sichuan (2023YFN0024, 2023NZZJ0015), and the High Impact Scholars Program of Sichuan University (SCU2022CG09).

Appendix A. Supporting information

Supplementary data associated with this article can be found in the online version at doi:10.1016/j.agwat.2026.110153.

Data availability

The authors do not have permission to share data.

References

Alizamir, M., Wang, M., Ikram, R.M.A., Ahmed, K.O., Heddam, S., Kim, S., 2024. An efficient computational investigation on accurate daily soil temperature prediction using boosting ensemble methods explanation based on SHAP importance analysis. Results Eng. 24. https://doi.org/10.1016/j.rineng.2024.103220.

Allen, R.G., Pereira, L.S., Raes, D., Smith, M., 1998. Crop evapotranspiration (Guidelines for computing crop water requirements). FAO Irrigation and Drainage Paper 56. FAO. Rome, Italy.

Al-Mahdawi, H.K., Alkattan, H., Subhi, A.A., Al-Hadrawi, H.F., Abotaleb, M., Ali, G.K., Mijwil, M.M., Towfeek, A.S.K., Helal, A.H., 2023. Analysis and prediction of evaporation rates using random forest models: a case study of almaty city. Babylon. J. Mach. Learn. 2023, 55–64.

Alonso, R., Elvira, S., Sanz, M.J., Gerosa, G., Emberson, L.D., Bermejo, V., Gimeno, B.S., 2008. Sensitivity analysis of a parameterization of the stomatal component of the DO$_3$SE model for Quercus ilex to estimate ozone fluxes. Environ. Pollut. 155 (3), 473–480. https://doi.org/10.1016/j.envpol.2008.01.032.

Ara, A., Maia, M., Louzada, F., Macêdo, S., 2022. Regression random machines: an ensemble support vector regression model with free kernel choice. Expert Syst. Appl. 202, 117107. https://doi.org/10.1016/j.eswa.2022.117107.

Buckley, T.N., 2019. How do stomata respond to water status? N. Phytol. 224 (1), 21–36. https://doi.org/10.1111/nph.15899.

Calderón-Orellana, A., Calderón-Orellana, M., Atenas, C., Contreras, C., Aburto, F., Alvear, T., Antileo-Mellado, S., 2025. Late water deficits improve intrinsic water use efficiency, fruit maturity, and acceptability in yellow-fleshed kiwifruit cv. Soreli. Plants 14 (18), 2843.

Carminati, A., Javaux, M., 2020. Soil rather than xylem vulnerability controls stomatal response to drought. Trends Plant Sci. 25 (9), 868–880. https://doi.org/10.1016/j.tplants.2020.04.003.

Dorogush, A.V., Ershov, V., Gulin, A., 2018. Catboost: gradient boosting with categorical features support [arxiv]. Arxiv, 7.

Dhawi, F., Ghafoor, A., Almousa, N., Ali, S., Alqanbar, S., 2025. Predictive modelling employing machine learning, convolutional neural networks (CNNs), and smartphone RGB images for non-destructive biomass estimation of pearl millet (Pennisetum glaucum). Front. Plant Sci. 16. https://doi.org/10.3389/fpls.2025.1594728.

Driesen, E., van den Ende, W., De Proft, M., Saeys, W., 2020. Influence of environmental factors light, co2, temperature, and relative humidity on stomatal opening and development: a review. Agron. Basel 10 (12). https://doi.org/10.3390/agronomy10121975.

Ellsäßer, F., Röll, A., Ahongshangbam, J., Waite, P., Hendrayanto, Schuldt, B., Hölscher, D., 2020. Predicting tree sap flux and stomatal conductance from drone-recorded surface temperatures in a mixed agroforestry system—a machine learning approach. Remote Sens 12 (24).

Elshaarawy, M.K., 2025. Stacked-based hybrid gradient boosting models for estimating seepage from lined canals. J. Water Process. Eng. 70, 106913. https://doi.org/10.1016/j.jwpe.2024.106913.

Elshaarawy, M.K., Alsaadawi, M.M., Hamed, A.K., 2024. Machine learning and interactive gui for concrete compressive strength prediction. Sci. Rep. 14 (1), 16694. https://doi.org/10.1038/s41598-024-66957-3.

Enouen, J., Liu, Y., 2025. Instashap: interpretable additive models explain shapley values instantly. Instashap: Interpretable Additive Models Explain Shapley Values Instantly.

Fernandes, R., Leblanc, S.G., 2005. Parametric (modified least squares) and non-parametric (theil-sen) linear regressions for predicting biophysical parameters in the presence of measurement errors. Remote Sens. Environ. 95 (3), 303–316. https://doi.org/10.1016/j.rse.2005.01.005.

Florek, P., Zagdański, A., 2023. Benchmarking state-of-the-art gradient boosting algorithms for classification. arXiv Prepr. arXiv 2308, 15114. ⟨https://arxiv.org/abs/2308.15114⟩.

Franks, P.J., Bonan, G.B., Berry, J.A., Lombardozzi, D.L., Holbrook, N.M., Herold, N., Oleson, K.W., 2018. Comparing optimal and empirical stomatal conductance models for application in earth system models. Glob. Change Biol. 24 (12), 5708–5723. https://doi.org/10.1111/gcb.14445.

Funk, J.L., Larson, J.E., Vose, G., 2021. Leaf traits and performance vary with plant age and water availability in Artemisia californica. Ann. Bot. 127 (4), 495–503. https://doi.org/10.1093/aob/mcaa106.

Gaur, S., Drewry, D.T., 2024. Explainable machine learning for predicting stomatal conductance across multiple plant functional types. Agric. For. Meteor. 350. https://doi.org/10.1016/j.agrformet.2024.109955.

Ge, T., He, K., Ke, Q., Sun, J., 2013. Optimized product quantization for approximate nearest neighbor search. 2013 IEEE Conference On Computer Vision and Pattern Recognition (Cvpr). IEEE, pp. 2946–2953.

Grossiord, C., Buckley, T.N., Cernusak, L.A., Novick, K.A., Poulter, B., Siegwolf, R.T.W., Sperry, J.S., Mcdowell, N.G., 2020. Plant responses to rising vapor pressure deficit. N. Phytol. 226 (6), 1550–1566. https://doi.org/10.1111/nph.16485.

Houshmandfar, A., O'Leary, G., Fitzgerald, G.J., Chen, Y., Tausz-Posch, S., Benke, K., Uddin, S., Tausz, M., 2021. Machine learning produces higher prediction accuracy than the Jarvis-type model of climatic control on stomatal conductance in a dryland wheat agro-ecosystem. Agric. For. Meteor. 304-305, 108423. https://doi.org/10.1016/j.agrformet.2021.108423.

Huang, Z., Liu, Y., Tian, F., Wu, G., 2020. Soil water availability threshold indicator was determined by using plant physiological responses under drought conditions. Ecol. Indic. 118, 106740. https://doi.org/10.1016/j.ecolind.2020.106740.

Hussein, A.H.K., Abouessaouab, M., 2023. Optimizing energy efficiency in smart grids using machine learning algorithms: a case study in electrical engineering. Khwarizmia 2023, 113–120.

Jalakas, P., Takahashi, Y., Waadt, R., Schroeder, J.I., Merilo, E., 2021. Molecular mechanisms of stomatal closure in response to rising vapour pressure deficit. N. Phytol. 232 (2), 468–475. https://doi.org/10.1111/nph.17592.

Jarvis, P.G., 1976. The interpretation of the variations in leaf water potential and stomatal conductance found in canopies in the field. Philos. Trans. R. Soc. B Biol. Sci. 273 (927), 593–610.

Jiang, S., Liang, C., Zhao, L., Gong, D., Huang, Y., Xing, L., Zhu, S., Feng, Y., Guo, L., Cui, N., 2022. Energy and evapotranspiration partitioning over a humid region orchard: field measurements and partitioning model comparisons. J. Hydrol. 610. https://doi.org/10.1016/j.jhydrol.2022.127890.

Lamptey, S., Li, L., Xie, J., Coulter, J.A., 2020. Tillage system affects soil water and photosynthesis of plastic-mulched maize on the semiarid Loess Plateau of China. Soil Tillage Res. 196, 104479. https://doi.org/10.1016/j.still.2019.104479.

Lawson, T., Vialet-Chabrand, S., 2019. Speedy stomata, photosynthesis and plant water use efficiency. N. Phytol. 221 (1), 93–98. ⟨https://10.1111/nph.15330⟩.

Li, C., Wang, N., Luo, X., Li, Y., Zhang, T., Ding, D., Dong, Q., Feng, H., Zhang, W., 2023. Introducing water factors improves simulations of maize stomatal conductance models under plastic film mulching in arid and semi-arid irrigation areas. J. Hydrol. 617. https://doi.org/10.1016/j.jhydrol.2022.128908.

Li, S., Liu, F., 2022a. Vapour pressure deficit and endogenous ABA level modulate stomatal responses of tomato plants to soil water deficit. Environ. Exp. Bot. 199, 104889. https://doi.org/10.1016/j.envexpbot.2022.104889.

Li, S., Tan, T., Fan, Y., Raza, M.A., Wang, Z., Wang, B., Zhang, J., Tan, X., Chen, P., Shafiq, I., Yang, W., Yang, F., 2022b. Responses of leaf stomatal and mesophyll conductance to abiotic stress factors. J. Integr. Agric. 21 (10), 2787–2804. https://doi.org/10.1016/j.jia.2022.07.036.

Lundberg, S., Lee, S.I., 2017. A unified approach to interpreting model predictions. https://10.48550/arXiv.1705.07874.

Martin-Stpaul, N., Delzon, S., Cochard, H., 2017. Plant resistance to drought depends on timely stomatal closure. Ecol. Lett. 20 (11), 1437–1447. https://doi.org/10.1111/ele.12851.

Matsumoto, K., Ohta, T., Tanaka, T., 2005. Dependence of stomatal conductance on leaf chlorophyll concentration and meteorological variables. Agric. For. Meteor. 132 (1-2), 44–57. https://doi.org/10.1016/j.agrformet.2005.07.001.

Miao, Y., Gao, G., Li, W., 2021. Environmental response and modeling of stomatal conductance of apple trees on the Loess Plateau. Arid Land Geogr. 44 (2), 525–533 (in Chinese).

Mills, T.M., Li, J., Behboudian, M.H., 2009. Physiological responses of gold kiwifruit (Actinidia chinensis) to reduced irrigation. J. Am. Soc. Hortic. Sci. 134 (6), 677–683. https://doi.org/10.21273/JASHS.134.6.677.

Mohammed, S., Arshad, S., Bashir, B., Ata, B., Al-Dalahmeh, M., Alsalman, A., Ali, H., Alhennawi, S., Kiwan, S., Harsanyi, E., 2024. Evaluating machine learning performance in predicting sodium adsorption ratio for sustainable soil-water management in the eastern Mediterranean. J. Environ. Manage. 370. https://doi.org/10.1016/j.jenvman.2024.122640.

Niazkar, M., Menapace, A., Brentan, B., Piraei, R., Jimenez, D., Dhawan, P., Righetti, M., 2024. Applications of xgboost in water resources engineering: a systematic literature review (dec 2018–may 2023). Environ. Modell. Softw. 174, 105971. https://doi.org/10.1016/j.envsoft.2024.105971.

Ortega-Farias, S., Poblete-Echeverria, C., Brisson, N., 2010. Parameterization of a two-layer model for estimating vineyard evapotranspiration using meteorological measurements. Agric. For. Meteor. 150 (2), 276–286. ⟨https://10.1016/j.agrformet.2009.11.012⟩.

Pan, Z., Fang, S., Wang, H., 2021. Lightgbm technique and differential evolution algorithm-based multi-objective optimization design of ds-apmm. Ieee Trans. Energy Convers. 36 (1), 441–455. https://doi.org/10.1109/TEC.2020.3009480.

Qi, Y., Zhang, Q., Hu, S., Wang, R., Wang, H., Zhang, K., Zhao, H., Zhao, F., Chen, F., Yang, Y., Tang, G., Hu, Y., 2023. Applicability of stomatal conductance models comparison for persistent water stress processes of spring maize in water resources limited environmental zone. Agric. Water Manag. 277, 108090. https://doi.org/10.1016/j.agwat.2022.108090.

Rahimi, M., Karbasi, M., Jamei, M., Rezaverdinejad, V., Malik, A., Farooque, A.A., Yaseen, Z.M., 2025. Meticulous estimation of maize actual evapotranspiration: a comprehensive explainable Catboost algorithm reinforced with jackknife uncertainty paradigm. Comput. Electron. Agric. 237. https://doi.org/10.1016/j.compag.2025.110599.

Rodriguez-Dominguez, C.M., Brodribb, T.J., 2020. Declining root water transport drives stomatal closure in olive under moderate water stress. N. Phytol. 225 (1), 126–134. ⟨https://10.1111/nph.16177⟩.

Rogiers, S.Y., Greer, D.H., Hatfield, J.M., Hutton, R.J., Clarke, S.J., Hutchinson, P.A., Somers, A., 2012. Stomatal response of an anisohydric grapevine cultivar to evaporative demand, available soil moisture and abscisic acid. Tree Physiol. 32 (3), 249–261. https://doi.org/10.1093/treephys/tpr131.

Samanta, S., Clayton, M.K., Mackay, D.S., Kruger, E.L., Ewers, B.E., 2008. Quantitative comparison of canopy conductance models using a Bayesian approach. Water Resour. Res. 44 (9). https://doi.org/10.1029/2007WR006761.

Saunders, A., Drew, D.M., Brink, W., 2021. Machine learning models perform better than traditional empirical models for stomatal conductance when applied to multiple tree species across different forest biomes. Trees For. People 6. https://doi.org/10.1016/j.tfp.2021.100139.

Sekeroglu, B., Ever, Y.K., Dimililer, K., Al-Turjman, F., 2022. Comparative evaluation and comprehensive analysis of machine learning models for regression problems. Data Intell. 4 (3), 620–652. ⟨https://10.1162/dint_a_00155⟩.

Sheridan, R.P., Wang, W.M., Liaw, A., Ma, J., Gifford, E.M., 2016. Extreme gradient boosting as a method for quantitative structure-activity relationships. J. Chem. Inf. Model 56 (12), 2353–2360. https://doi.org/10.1021/acs.jcim.6b00591.

Sun, R., Ma, J., Sun, X., Bai, S., Zheng, L., Guo, J., 2023. Study on a stomatal conductance model of grape leaves in extremely arid areas. Sustainability 15 (10), 8342.

Wang, Q., He, Q., Zhou, G., 2018. Applicability of common stomatal conductance models in maize under varying soil moisture conditions. Sci. Total Environ. 628-629, 141–149. https://doi.org/10.1016/j.scitotenv.2018.01.291.

Wang, S., Qiu, Y., Zhu, F., 2021. Kiwifruit (Actinidia spp.): A review of chemical diversity and biological activities. Food Chem. 350, 128469. https://doi.org/10.1016/j.foodchem.2020.128469.

Whitehead, D., 1998. Regulation of stomatal conductance and transpiration in forest canopies. Tree Physiol. 18 (8-9), 633–644. https://doi.org/10.1093/treephys/18.8-9.633.

Wu, X., Xu, Y., Shi, J., Zuo, Q., Zhang, T., Wang, L., Xue, X., Ben-Gal, A., 2021. Estimating stomatal conductance and evapotranspiration of winter wheat using a

soil-plant water relations-based stress index. Agric. For. Meteor. 303, 108393. https://doi.org/10.1016/j.agrformet.2021.108393.

Yu, F., Isleem, H.F., Almoghayer, W.J.K., Shahin, R.I., Yehia, S.A., Khishe, M., Elshaarawy, M.K., 2025. Predicting axial load capacity in elliptical fiber reinforced polymer concrete steel double skin columns using machine learning. Sci. Rep. 15 (1), 12899. https://doi.org/10.1038/s41598-025-97258-y.

Zheng, S., Jiang, S., Cui, N., Zhao, L., Gong, D., Wang, Y., Wu, Z., Liu, Q., 2023. Deficit drip irrigation improves kiwifruit quality and water productivity under rain-shelter cultivation in the humid area of South China. Agric. Water Manag 289, 108530. https://doi.org/10.1016/j.agwat.2023.108530.

Zheng, S., Cui, N., Gong, D., Wang, Z., Chen, F., Liu, Q., Jiang, S., 2025. Optimization of kiwifruit irrigation strategies using multi-objective optimization algorithms coupled with water production functions. Comput. Electron. Agric. 237. https://doi.org/10.1016/j.compag.2025.110579.